Advanced Materials Science and Technology Vol 6 Issue 1 2024
DOI: 10.37155/2717–526X–0601–6

REVIEW

Open Access

Omniscient Pte.Ltd.

Advancements and Challenges of P2 Na_xTMO_2 (TM = Mn, Ni, Co, Fe, Cu) Cathodes for High-performance Sodium-ion Battery

Hongrui Yu[1], Chengping Li[1,2,*], Peng Dong[2], Jinsong Wang[1], Zhengfu Zhang[1], Yingjie Zhang[2], Jiangzhao Chen[1,*]

[1]Faculty of Materials Science and Engineering, Kunming University of Science and Technology, Kunming 650093, P. R. China
[2]Faculty of Metallurgical and Energy Engineering, Kunming University of Science and Technology, Kunming 650093, P. R. China

***Correspondence to:** Chengping Li, Faculty of Materials Science and Engineering, Kunming University of Science and Technology, Kunming 650093, P. R. China. Faculty of Metallurgical and Energy Engineering, Kunming University of Science and Technology, Kunming 650093, P. R. China. Email: li.cp@kust.edu.cn; Faculty of Materials Science and Engineering, Kunming University of Science and Technology, Kunming 650093, P. R. China. Email: jzchen@kust.edu.cn.

Received: May 15, 2024; **Accepted:** August 14, 2024; **Published Online:** August 23, 2024

Citation: Yu HR, Li CP, Dong P, Wang JS, Zhang ZF, Zhang YJ, et al. Advancements and Challenges of P2 Na_xTMO_2 (TM = Mn, Ni, Co, Fe, Cu) Cathodes for High-performance Sodium-ion Battery. *Advanced Materials Science and Technology*. 2024, 6(1): 0633312. https://doi.org/10.37155/2717-526X-0601-6

Abstract: Sodium-ion batteries have become one of the most promising options for large-scale energy storage due to their abundant sodium source, high storage capacity and relatively low price. Among the key components of sodium-ion batteries, cathode materials play a pivotal role and have a significant impact on the energy density and power density of the battery. Advances in cathode materials ultimately determine the practical applications of sodium-ion batteries. The P2-type layered transition metal oxides have open Na^+ diffusion channels, and Na^+ can migrate through the adjacent trigonal positions, resulting in high diffusion coefficients, giving them good rate and cyclic properties. However, in P2-type layered transition metal oxide cathode materials, there are several challenges, such as structural distortion, irreversible oxygen atom redox at high voltages, and irreversible phase transitions, which seriously affect the rate and cycling performance of the batteries. As a result, these issues have hindered the widespread application of sodium-ion batteries in large-scale energy storage. It is crucial to optimize the P2-Na_xTMO_2 layered transition metal oxide cathode materials. This review summarizes the challenges and research progress of P2-Na_xTMO_2 layered transition metal oxide cathode materials for the development of P2-Na_xTMO_2 cathodes for high-energy sodium-ion batteries.

Keywords: Sodium-ion batteries; Cathode materials; P2-Na_xTMO_2; Challenges; Research progress

1. Introduction

The demand for fossil fuels continues to increase with the rapid development of modern society. Burning fossil fuels generates the greenhouse effect, which causes global warming and sea level rise, posing a significant threat to the ecological balance of the earth[1,2]. The achievement of carbon neutrality is a key initiative in the fight against global warming[3]. Adjusting the energy structure to gradually transition from traditional fossil fuels to renewable energy sources is crucial in achieving the goal of carbon neutrality[4-7].

Renewable and environmentally friendly energy sources, such as wind, sun, and tides, have gained significant attention. However, these sources are subject to seasonal variations and are characterized by intermittency, transience, and uneven distribution, which make their direct use challenging. Therefore, there is a requirement to develop efficient large-scale energy storage systems that can be used on demand. As a result, large-scale electrochemical energy storage and conversion technologies, such as secondary batteries, have become a popular research area[8-11].

Lithium-ion batteries (LIBs) are a type of secondary rechargeable battery used for storing and converting electricity. They are known for their high energy density, efficiency, and cycling stability, making them a popular choice for portable electronic products and new energy vehicle power supplies. However, the use of combustible organic electrolytes and the thermal runaway caused by the reaction between electrode materials and electrolytes, pose a significant safety risk for LIBs. Additionally, issues such as the uneven distribution of lithium resources and high costs are increasingly hindering the application of LIBs in large-scale energy storage systems[12-14]. Thus, to achieve sustainable electrochemical energy storage and conversion on a large scale, it is imperative to identify an alternative energy storage system to replace LIBs as secondary batteries.

Sodium metal shares physicochemical properties with lithium metal. Additionally, sodium-ion batteries (SIBs) have their own advantages. Sodium resources (2.36 wt%) rank the 6th in terms of natural reserves, which is more advantageous in terms of reserves and makes the cost lower compared to lithium resources (0.0017 wt%), which rank the 27th in terms of natural reserves in the earth's crust[15]. Secondly, it is worth noting that Na^+/Na (−2.71 V) has a similar standard electrode potential to Li^+/Li (−3.04 V), with only a 0.33 V difference[16]. Additionally, Na^+ have a smaller Stokes radius than Li^+, resulting in higher conductivity. Finally, SIBs can use aluminum foil as a collector, which is less expensive than the copper foil used in LIBs, making commercialization more feasible[17]. SIBs are considered a more desirable alternative chemical energy system to LIBs due to their lower cost and greater abundance of sodium.

Cathode material is a crucial component of SIBs, and the performance of secondary batteries is limited by the development of cathode materials. Therefore, research into cathode materials for secondary batteries is key to improving their performance. Cathode materials for SIBs can be classified into three main categories: layered transition metal oxides, polyanion-type compounds, and Prussian blue compounds[18-20]. Polyanionic compounds are compounds that contain anionic tetrahedra or their derived groups as structural units $(XO_m)^{n-}$ (where X represents elements such as P, S, V, and W) with an open framework consisting of transition-metal-oxygen polyhedral. These compounds are thermally stable due to the X-O covalent bonding in the structure and the presence of a large number of vacancies in the structure, which makes the volume changes and phase transitions in the process of Na^+ removal/intercalation relatively weak. The inclusion of X in polyanionic compounds results in a high redox potential due to its induced effect[21]. However, the unique structure of polyanions results in lower conductivity and theoretical energy density, as well as a lower charge/discharge plateau[21-24]. The Prussian blue analogue is a complex formed by transition metal ions and cyanogen ions (CN^-) through coordination. It has a three-dimensional open framework structure that is favorable for Na^+ detachment and intercalation during the charging and discharging process. Additionally, it has the advantages of high energy density, small volume change, and good rate performance. However, the presence of water in its structure can cause side reactions with the organic electrolyte, leading to a

deterioration in electrochemical performance. This results in poor cycling stability, which hinders its practical application[25-28].

Layered transition metal (TM) oxides are considered the most promising cathode materials for SIBs due to their high theoretical capacity, high ionic conductivity, simple synthesis process, simple structure, and environmental friendliness[29-32]. The chemical formula for these oxides is Na_xTMO_2, where TM represents one or more transition metal elements such as Ni, Co, Mn, Fe, Cu, etc., and $0 < x \leqslant 1$[33]. The material consists of atoms of transition metal elements and Na^+ arranged in a specific coordination manner. Delmas et al.[34] classified the material based on the position of the sodium ion in either trigonal prisms (P-type) or octahedra (O-type), depending on the content and mode of occupancy of the sodium ions. The P-type can be further subdivided into the P2 and P3 types, which exhibit edge-sharing and face-sharing connections in their respective crystal structures. Similarly, the O-type can be subdivided into the O2 and O3 types, which also display edge-sharing connections in their crystal structures. The numbers 2 and 3 refer to the number of TM layers present in the stacked repeating unit. The P2 and P3 types of oxygen are arranged in an alternating pattern, ABAB and ABBCCA, respectively; the P2-type structure are classified as the 2H phase with a space group of P63/mmc. Na1 (Na_e) and Na2 (Na_f) are the two distinct triclinic positions occupied by sodium ions in the P2 type. Na1 is bonded to two adjacent TMO_6 octahedral slabs in a shared-edge manner, while Na2 binds to the six surrounding TMO_6 octahedra in a shared surface manner. In contrast, the O2 and O3 types are stacked in an ABAC and ABCABC manner, respectively. The O3-type layered structure is classified as a 3R phase with a space group R-3m. In this structure, transition metal and sodium ions are located at different octahedral positions in the cubic densely stacked oxygen arrays of the O3-type phases. Furthermore, TMO_6 octahedra sharing the edges and NaO_6 are arranged in alternating layers in the O3-type material along the [111] direction. This results in the formation of TMO_2 and NaO_2 plates. Subsequently, three separate TMO_2 layers (AB, CA, and BC) were stacked to form a layered O3-type structure[33]. In general, the P2 and O3 phases undergo a series of phase transitions during charge/discharge cycling, including different stacking sequences of the oxide layers. As illustrated in **Figure 1a-b**, the de-intercalation of a specific quantity of Na^+ results in the sliding ($\pi/3$ rotation) of certain TMO_6 octahedral sheets. This process typically transforms the P2 phase into the O2 phase, which causes a notable contraction of the crystal structure and a reduction in the interlayer distance. As illustrated in **Figure 1b**, the presence of Na^+ within the P2-type phase stabilizes the larger prismatic positions. Consequently, following Na^+ de-intercalation[35], the TMO_2 sheets slide (move) to form octahedral positions, thereby leading to the formation of a new O2 phase with AB AC AB oxygen stacking, which is achieved through Na^+ exchange[36]. The O2 phase crystallographically comprises two distinct TMO_2 sheets with AB and AC oxygen arrangements, with vacancies remaining between the AB and AC layers. Consequently, the O2-type layered phase is classified as a hexagonal close-packed (hcp) oxygen array containing both ABA-type and ACA-type (**Figure 1b**) oxygen arrangements. In contrast to the O3-type phases with hcp arrays (ABC-type oxygen arrangements) discussed in the previous section, the NaO_2 and TMO_2 layers on both sides only share edges. The O2-type phase can be categorised as a symbiotic structure between ccp and hcp arrays based on the oxygen stacking. The nucleation of the O2 phase within the P2 microcrystals can occur in several portions of the crystals with two sliding vectors (2/3, 1/3, 0) and (1/3, 2/3, 0), resulting in the formation of extended defects at the boundaries between the individual domains. In the O3-type phase, however, Na^+ initially occupies an octahedral position shared with the TMO_6 octahedra, as illustrated in **Figure 1c**. Upon partial de-intercalation of Na^+ from the O3-type phase, Na^+ in prismatic positions becomes energetically stable, accompanied by the formation of vacancies, which is similar to the P2-type phase Subsequently, the formation of broad prismatic sites was achieved through the sliding of TMO_2 sheets without the disruption of the TM-O bond. This process resulted in the oxygen stacking becoming "AB BC CA," thereby forming the P3 phase (**Figure 1d**)[37].

The most commonly used crystal structures in Na_xTMO_2 materials are the O3 and P2 phases. The O3 type layered oxides have a high theoretical capacity. However, the complex phase transition during the charge/discharge process leads to structural instability,

resulting in lower reversible capacity and poor cycling capacity retention[38]. P2-type layered transition metal oxides enable direct migration of Na^+ through neighboring triangular prism Na sites, resulting in a faster Na^+ migration rate and better cycling and multiplicity performance. Therefore, P2-Na_xMnO_2 compounds are of particular interest[39].

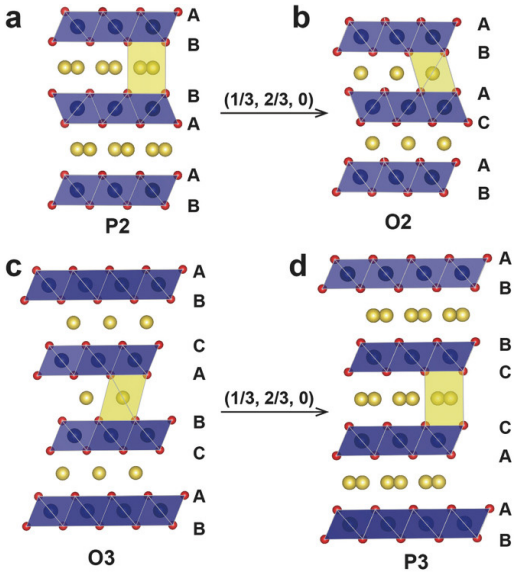

Fig 1. A schematic of the crystal structures for Na_xTMO_2. (a) P2-type stacking. (b) O2-type stacking. (c) O3-type stacking. (d) P3-type stacking. The blue and yellow balls represent the transition metal and Na ions in the O-type frameworks, respectively. Reproduced with permission[37]. Copyright 2018, Wiley.

The crystal structures of P2-type and O3-type layered oxides can be distinguished based on the ratio between the interlayer distance d(O-Na-O) of the Na metal layer and the TM layer distance d(O-TM-O). A ratio of approximately 1.62 distinguishes between P2-type and O3-type oxides[40]. The larger proportion of P2-type oxides is derived from a more localized electron distribution within the TMO_2 plate, which results in a weaker repulsion between adjacent NaO_2 plates. This, in turn, leads to a stronger repulsion between adjacent TMO_2 plates. This indicates that the distribution of electrons plays a significant role in the competition between P-type and O-type stacking in layered oxides. The ionic potential (Φ) is an indicator of the charge density on the surface of the ion. This is calculated as the ratio of the charge number (n) to the ionic radius (R), reflecting the cation polarizability. The ionic potential demonstrates the anticipated increase with rising oxidation state and atomic mass. In order to provide a simple description of layered oxides, Hu's group expressed the degree of cation electron density and its polarizability by introducing a "cation potential" normalized to the ionic potential of the anion (O):

$$\Phi_{cation} = \frac{\overline{\Phi_{TM}}\,\overline{\Phi_{Na}}}{\overline{\Phi_{O}}} \quad (1)$$

where $\overline{\Phi_{TM}}$ represents the weighted average ionic potential of the TMs, defined as $\overline{\Phi_{TM}} = \sum \frac{w_i n_i}{R_i}$; w_i is the content of the TM_i, n_i is the number of charges and R_i is the radius; and $\overline{\Phi_{Na}}$ represents the weighted average ionic potential of the Na, $\overline{\Phi_{Na}} = \sum \frac{x}{R_{Na}}$. The charge balance in the Na_xTMO_2 composition requires $\sum w_i n_i = 4-x$, where x represents the Na content and 4 represents the total oxidation state to compensate for the O^{2-} charge.

The cation potential provides an accurate description of the interplate interactions and, as a result, of the competition between P2-type and O3-type structures. A larger cation potential ((Equation 1) is indicative of a more extended TM electron cloud and stronger interlayer electrostatic repulsion, which results in the formation of a P2-type structure with a greater number of covalent TM-O bonds and a larger d(O-Na-O) distance. Conversely, the greater Na ion-averaged potential obtained by increasing the Na content increases the shielding against electrostatic

repulsion between the TMO_2 laminae, thereby favoring the formation of O3-type structures. Even minor differences in TM or Na content can result in a transition between P2-type and O3-type structures. The cation potential can be employed as a guide for the design of specific stacking structures by controlling the Na content and TM composition. High Na-content layered oxide crystal structures with $x > 0.67$ are typically O3-type structures. However, by increasing the cation potential, it is possible to obtain P2-type structures with high Na content. As a case in point, $NaLi_{1/3}Mn_{2/3}O_2$ can be taken as an example, where the cation potential can be increased in order to avoid the formation of the O3 phase (Equation 1). Firstly, it is assumed that the Na content remains constant, which can be achieved by increasing the ionic potential at the TM site. According to the cationic potential, a P2-type structure with $x = 1$ ($\overline{\Phi_{Na}} = 9.8$) would require a very large TM ionic potential, which is, however, larger than the ionic potential in the widely used TM with a maximum in Mn^{4+}. Accordingly, the Na content in $NaLi_{1/3}Mn_{2/3}O_2$ must be diminished while compensating for this by reducing the Li and increasing the charge of the Mn content. The compositions $Na_{5/6}Li_{5/18}Mn_{13/18}O_2$ with high Na content, which were successfully predicted to have a P2-type structure based on the cation potential, were successfully prepared experimentally. It was similarly demonstrated that lowering the cation potential allows the synthesis of an O3-type structure with a low Na content, as exemplified by the preparation of $Na_{2/3}Mg_{1/3}Ti_{2/3}O_2$[41].

Although the energy density of P2-type layered oxides is inferior to that of O3-type structures, they exhibit superior structural integrity, long cycle stability, and rate performance. Therefore, P2-type layered oxides are likely to become the next generation of cathode materials for commercial SIBs.

This paper reviews recent research progress on P2-type layered transition metal oxides for SIBs. Specifically, it summarizes the problems associated with these oxides and several strategies to modify and enhance their electrochemical properties. Layered sodium transition metal oxides (Na_xTMO_2) are strong candidates for cathode.

2. The Challenge of P2-Na_xTMO_2 Layered Transition Metal Oxides

Although P2-Na_xTMO_2 layered transition metal oxides have several advantages, such as high theoretical specific capacity, rate performance, and low cost. However, P2-Na_xTMO_2 material faces some challenges: structural evolution, structural distortions caused by the Jahn-Teller effect, irreversible oxygen atom redox reactions, and migration and dissolution of transition metals.

2.1 Structural evolution

Ideally, P2 layered transition metal oxides should maintain a P2-type structure during the charge-discharge process, with minimal structural volume changes during sodium ion de-intercalation and intercalation. However, in practice, sodium ions become de-intercalated within the material during charging and discharging, resulting in changes to the sodium ion content and various phase transitions. Using $Na_{2/3}Ni_{1/3}Mn_{2/3}O_2$ as an example, the P2 structure is maintained when the sodium content is between 2/3 and 1/3. When the sodium content is less than one-third, the shielding effect of sodium ions weakens. This weakens the electrostatic attraction between the oxygen layers, causing the neighboring transition metal layers to slip. Additionally, the sodium ions change from the original triangular prismatic sites to the octahedral sites, and the stacking order of the transition metal layers changes from ABBA to ACAC. The stacking order of the transition metal layer changes from ABBA to ACAC, resulting in the formation of an O2 phase with a contracted crystal structure and reduced layer spacing[42,43]. This leads to a volume change of approximately 23.2%[44].

In the two-phase reaction, stress is generated at the interface, and the probability of crack nucleation at this location increases with the difference between the two phases. When charging the $Na_{2/3}Mn_{2/3}Ni_{1/3}O_2$ material to 4.2 V, there is always a region of preferentially detached sodium ions due to incomplete and non-uniform detachment from the crystal lattice. When most of the sodium ions are removed from this region, a large number of vacancies aggregate, causing the original P2-type structure to gradually transform into the O2 phase. This transformation results in a significant stress concentration at the interface between the original P2 phase and the transformed O2 phase. During the cycling process, the material experiences repeated stress concentration and relief as sodium ions are extracted and intercalated. This can induce

cracks on the surface of the particles at the interface of the two phases. During the charging and discharging process, cracks continue to expand into the interior of the particles, eventually forming cracks throughout the particles. This greatly damages the material's structure and reduces its performance (**Figure 2a-c**). **Figure 2d** shows that stress concentration occurs during the charging and discharging process when a two-phase reaction with a large difference takes place. This is usually followed by crack nucleation, and the tip of the nucleated crack extends to the inside of the grain due to the coupling effect of the cathode/electrolyte side reaction. This is accompanied by the migration of sodium ions into the electrolyte and the solubilization and migration of the transition metal at the tip of the crack[45].

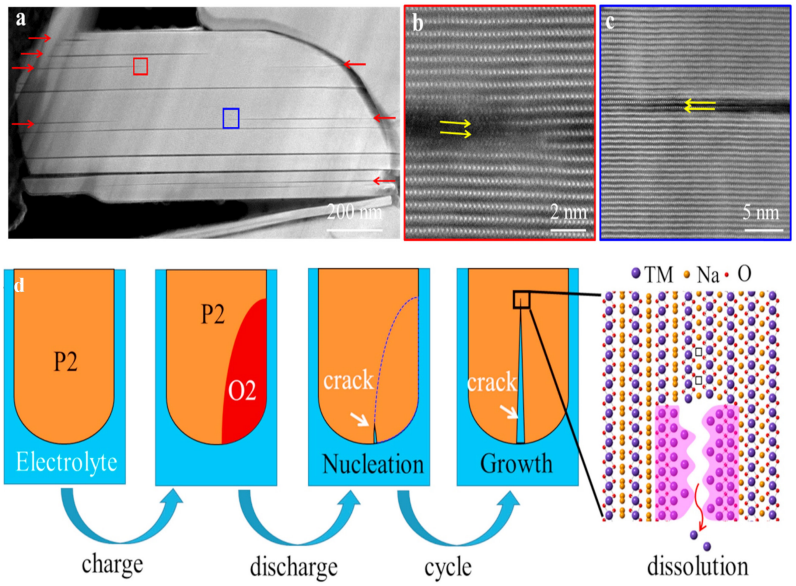

Fig 2. Nucleation and growth of intragranular cracks. (a) intragranular cracks were observed at the grain level of the sample after 50 cycles using a scanning transmission electron microscope-high angle annular dark field (STEM-HAADF) at 2.0-4.25 V. The cracks were located inside the grain. The red arrow highlights the crack with the crack tip located inside the grain. (b-c) are dot-matrix images from the red and blue frames in (a). The yellow arrows in (b) and (c) highlight the two missing plates. (d) schematic representation of crack nucleation and growth. Reproduced with permission [45]. Copyright 2018, Elsevier.

P2-type layered oxides have three known ordering processes: (1) transition metal ion ordering[46]; (2) transition metal ion charge ordering[47]; and (3) Na^+/vacancy ordering[48-50]. The ordering of Na^+/vacancy is favored due to the strong Na^+-Na^+ repulsion in the alkali metal (AM) layer and the charge ordering in the transition metal layer. The material undergoes multiple ordered/disordered multiphase transitions, which correspond to multiple step-like voltage drops in the charge/discharge curves due to the ordering of sodium ions/vacancies forming a superlattice phase. The slow sodium ion transport kinetics are caused by the structural ordering[51], which may also couple with structural transitions, leading to structural instability and severely affecting the cycling performance[52]. Ordering of Na^+/vacancy can be effectively suppressed by constructing transition metal components with similar ionic radii[53]. This disruption facilitates the transformation of the original two-phase reaction of the material to a solid-solution reaction, which improves the material's stability during cycling, especially when the original two-phase reaction of the material is significantly different.

The charging and discharging process causes structural evolution, resulting in changes in structural volume. This generates constant stress changes, leading to particle fragmentation and detachment of active material from the electrode sheet. As a result, properties such as specific capacity and cycling stability degrade. Suppressing volume change during charging and discharging is essential for synthesizing low-strain cathode materials.

2.2 Structural distortions caused by the Jahn-Teller effect

The Jahn-Teller effect was proposed by Jahn and Teller in 1937, hence its name, the Jahn-Teller effect. The theory proposes that any nonlinear molecule with a spatially-simple electronic ground state and in which the electrons exhibit asymmetric occupation in the simplex orbitals will result in the splitting of the simplex energy levels, as well as a change in the spatial arrangement of the atoms in the molecule (geometrical aberration), which reduces the symmetry of the molecule and the total energy of the system. The alteration results in a decrease in system energy and promotes a shift towards a more stable state. As a consequence, the Jahn-Teller effect occurs spontaneously[54]. According to ligand field theory, theoretically there are five simplicial orbitals in the d-orbitals, however, practically in octahedral complexes, the d-orbitals contain the triple simplicial orbitals, t_{2g} (d_{xy}, d_{zx}, and d_{xy}), as well as the dual simplicial orbitals, e_g (d_z^2 and $d_{x^2-y^2}$), where the e_g orbitals have slightly higher energy than the t_{2g} orbitals. As shown in **Figure 3**, the Jahn-Teller effect is more likely to occur in octahedral complexes with nine d-electrons (d^9), low-spin d^7 and high-spin d^4 metal electrons, such as Mn^{3+} in the high-spin state, Ni^{3+} and Cu^{2+} in the low-spin state.

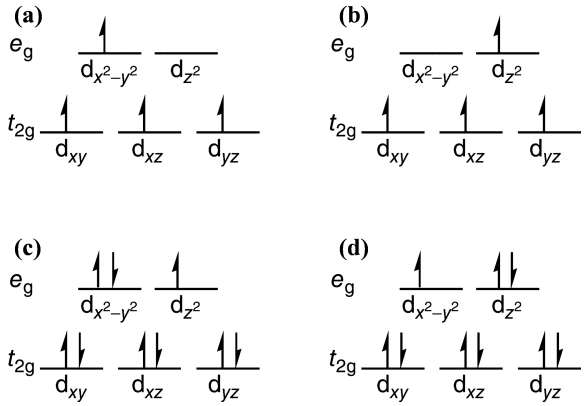

Fig 3. Presentation of the two possible ways of electron filling of the d orbitals. (a-b) high-spin d^4 octahedral metal complexes. (c-d) d^9 octahedral metal complexes. Reproduced with permission [55]. Copyright 2013, American Chemical Society.

For example, in the case of a high-spin d^4 (Mn^{3+}) complex, there is a vacancy in either the $d_{x^2-y^2}$ or d_z^2 orbital, as shown in **Figure 3a-b**. There are two possible ways to fill these orbitals, $d^1_{x^2-y^2}d^0_{z^2}$ or $d^0_{x^2-y^2}$ $d^1_{z^2}$, both with equal energy. Similarly, for the d^9 metal complex shown in **Figure 3c-d**, there are two ways to occupy the orbitals, $d^2_{x^2-y^2}$ $d^1_{z^2}$ or $d^1_{x^2-y^2}d^2_{z^2}$, both of equal energy. Jahn and Teller argued that the electron distribution is unstable, causing the octahedron to distort and lower the symmetry. This results in unequal energies for the two mentioned electron configurations. Using the configurations of $d^0_{x^2-y^2}$ $d^1_{z^2}$ (d^4) and $d^1_{x^2-y^2}$ $d^2_{z^2}$ (d^9) as an example, it is observed that the ligand(s) on the z-axis have a stronger charge shielding effect on the central metal ion compared to the other four ligands on the x-axis and y-axis. This is due to the concentration of electron density in the d_z^2 orbitals on the z-axis between the metal and the two ligands. The electrostatic repulsion between the electron(s) in the d_z^2 orbital and the ligand on the z-axis is greater than that between the electrons in the t_{2g} orbitals pointing between the axes and the ligands on the x- and y-axes. This causes the ligand on the z-axis to move further away from the central metal ion due to the strong electrostatic repulsion, resulting in a reduction of symmetry (z-out or extended Jahn-Teller distortion). The proposed change will result in a decrease in the energy of the d_z^2 orbital and an increase in the energy of the $d_{x^2-y^2}$ orbital, making the d_z^2 orbital more stable[54]. **Figure 4** shows that aberrations can be expected from the $d^2_{x^2-y^2}$ $d^1_{z^2}$ (d^9) and $d^1_{x^2-y^2}$ $d^0_{z^2}$ (d^4) configurations, which are z-in or compressed Jahn-Teller aberrations[56]. The z-out or elongated Jahn-Teller distortion leads to a lengthening of the M-L bond in the z-axis or a shortening of the bond length in the x- and y-axes. Specifically, the z-in or compression distortion shortens the length of the M-L bond on the z-axis, while the x and y axes experience lengthening of the

M-L bond. The Jahn-Teller effect causes geometric distortions of the octahedron[55,57].

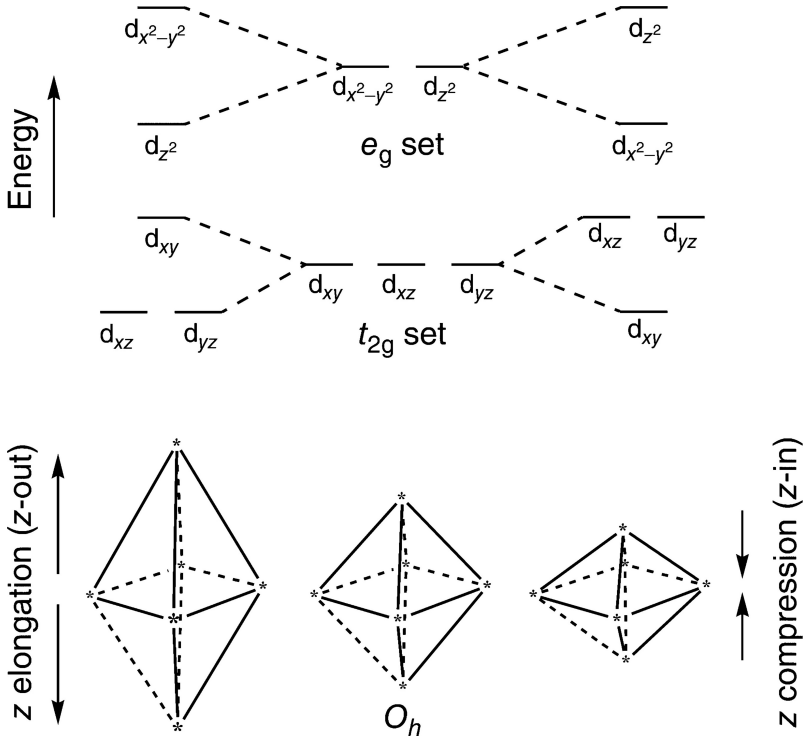

Fig 4. The effect of z elongation and compression Jahn-Teller distortion on the M-L bond lengths and energy of the e_g and t_{2g} set of orbitals. Reproduced with permission[55]. Copyright 2013, American Chemical Society.

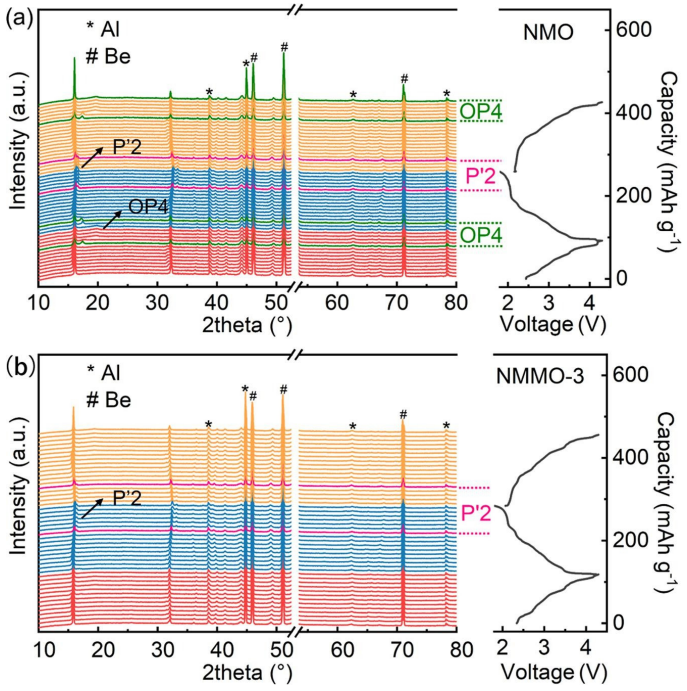

Fig 5. In-situ XRD patterns corresponding to the charge/discharge curves of (a) NMO and (b) NMMO-3 in a voltage of 1.8-4.3 V. Reproduced with permission[58]. Copyright 2021, Elsevier.

The P2-P'2 phase transition process is typically regarded as being closely associated with the strong Jahn-Teller effect induced by the Mn^{3+}/Mn^{4+} redox couple in Na_xMnO_2 electrodes. This results in severe

structural distortion, which in turn reduces Na^+ mobility and further leads to stresses and structural defects. Zhang et al.[58] employed in situ XRD to investigate the structural evolution of $Na_{0.67}MnO_2$ (NMO) and $Na_{0.67}Mn_{0.97}Mo_{0.03}O_2$ (NMMO-3) during charge-discharge cycling. As illustrated in **Figure 5a**, the (002) and (004) peaks split into two peaks at a discharge voltage of 2.3 V. This phenomenon can be attributed to the increase in Jahn-Teller active Mn^{3+}, which results in structural distortion and the formation of the rhombohedral crystalline P'2 phase. As illustrated in **Figure 5b**, the peaks of the OP4 phase do not emerge in NMMO-3 until charging to 4.3 V. During discharge, the (002) and (004) peaks undergo a shift to a larger angle. This suggests that the subphase transition of P2-OP4 was inhibited by the doping of Mo. Furthermore, the peak of the P'2 phase emerged at 1.09 Na^+ insertion into the molybdenum-doped compound and subsequently disappeared reversibly. The suppression of the Jahn-Teller distortion of Mn^{3+} is indicated based on the weakening of the P'2 phase peak. This indicates that the phase transition in NMMO-3 is highly reversible, while that of P2-OP4 is suppressed.

The structural changes in $Na_{0.67}Fe_{0.5}Mn_{0.5}B_{0.04}O_2$ (NFMO-B) and $Na_{0.67}Fe_{0.5}Mn_{0.5}O_2$ (NFMO-P) during Na^+ detachment and intercalation were investigated by in-situ XRD and refinement of their results by Fang et al.[59] The octahedral distorted structure of MnO_6 induced by the Jahn-Teller effect is reacted in the atomic structure. The bond lengths of NFMO-P and NFMO-B in different states are presented in **Figure 6a-d**, and the corresponding data are compared in **Figure 6e**. The results indicate that NFMO-B exhibits a lower rate of variation and distortion of the TM-O bond length along the z-axis compared with NFMO-P. Consequently, the stress and structural defects of NFMO-B during long cycling are effectively alleviated, which contributes to the cycling stability of the material.

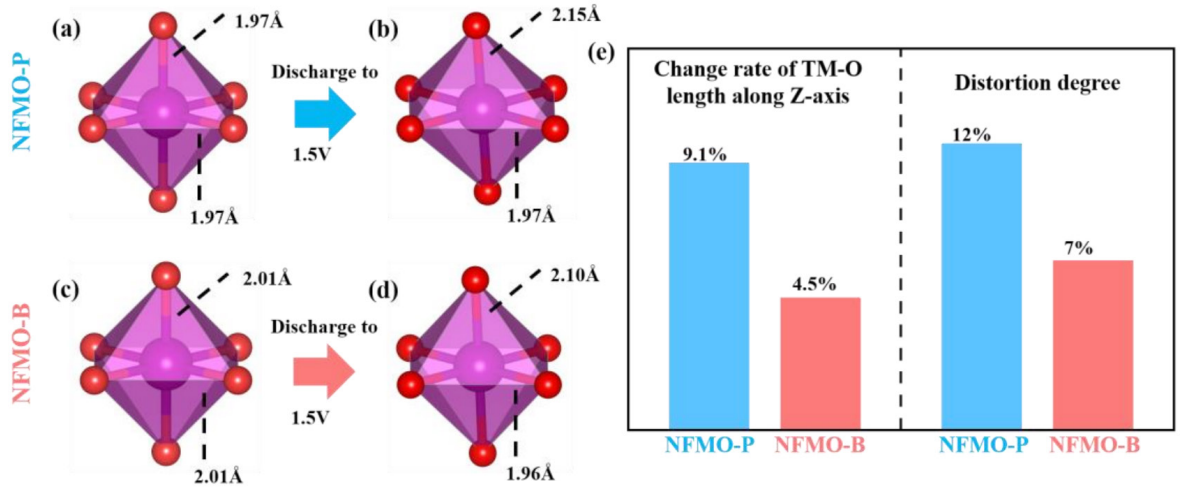

Fig 6. Illustration of Jahn-Teller octahedron distortion for (a-b) NFMO-P and (c-d) NFMO-B. (e) Comparison of distortion degree. Reproduced with permission[59]. Copyright 2023, Wiley.

The Jahn-Teller effect causes structural distortion, which can harm the structural stability and electrochemical properties of materials. To minimize these adverse effects, it is generally recommended to avoid or reduce the incorporation of Jahn-Teller effect active elements or active valence ions during the material design stage.

2.3 Irreversible oxygen atom redox reactions

The cathode material is composed of a transition metal layer and a sodium ion layer arranged in a specific order. Charge transfer occurs through the redox of the transition metal element during the charging/discharging process, which involves the shedding/intercalation of sodium ions. Examples of transition metal elements involved in this process include $Mn^{2+}/Mn^{3+}Mn^{4+}$, $Ni^{2+}/Ni^{3+}Ni^{4+}$, and Fe^{4+}/Fe^{3+}. The amount of energy that the cathode material can provide depends on the transferred charge resulting from the change in valence state after the redox of the transition metal elements. However, in practice, many oxide cathode

materials provide a specific capacity during charging and discharging that exceeds the theoretical capacity of the transition metal elements. This is believed to be due to the redox of oxygen in the crystal lattice under certain conditions, resulting in the loss of electrons and providing additional capacity beyond the theoretical limit[60,61]. The phenomenon of unexpectedly high specific capacities in lithium-rich materials was first discovered. Subsequent studies revealed that the additional capacity was provided by redox reactions of oxygen atoms in the lattice[62-65].

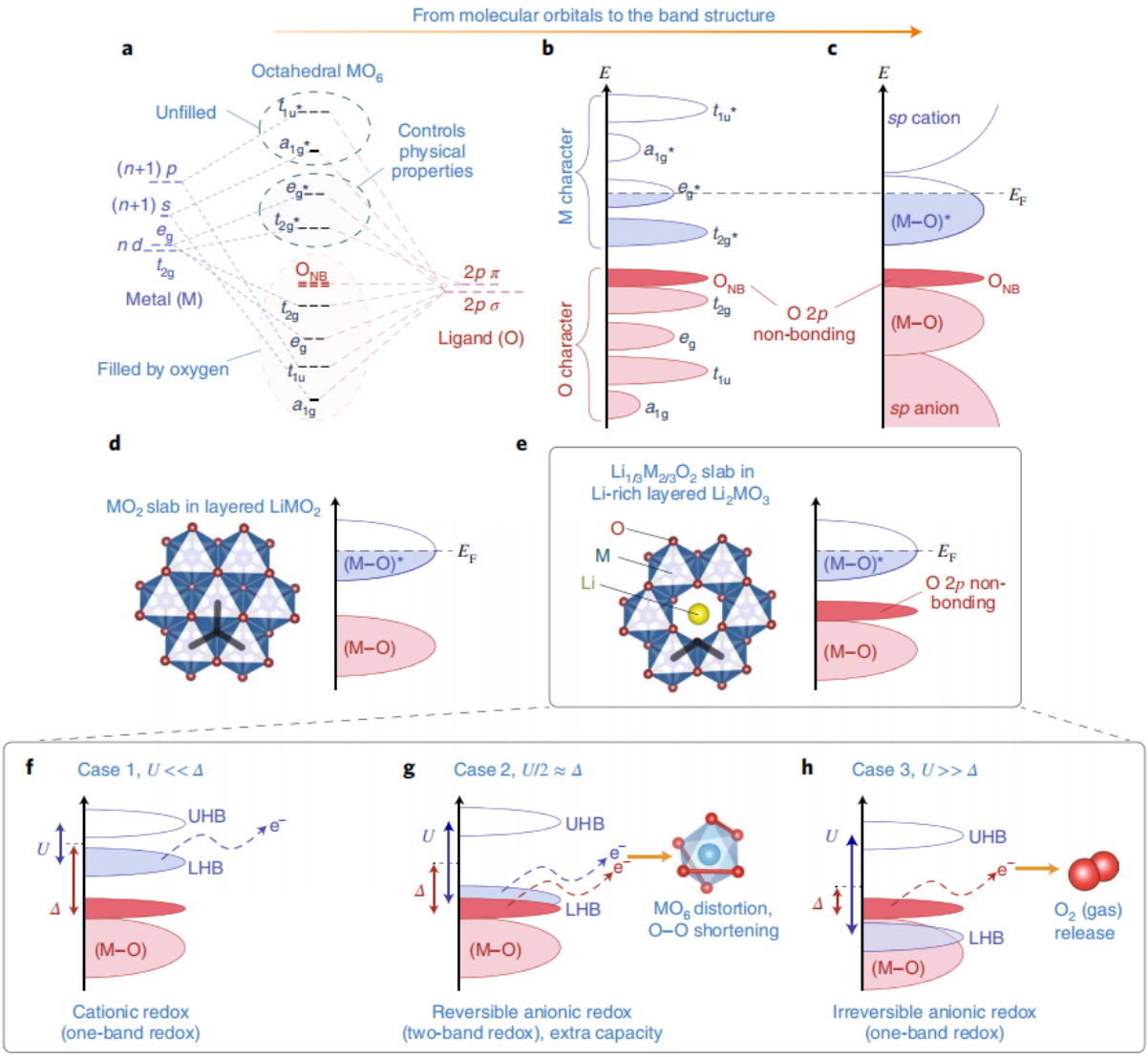

Fig 7. Band structure of oxides and the anionic redox mechanism. (a-c) transition metal oxide schematic energy band structure. (d) $LiMO_2$ crystal structure and its energy band structure. (e) Lithium-rich Li_2MO_3 crystal structure and its energy band structure. (f-h) considering the Mott-Hubbard splitting, the three energy band structures of Li_2MO_3. Reproduced with permission[61]. Copyright 2018, Springer Nature Limited.

The subsequent section will describe the mechanism by which oxygen atoms undergo redox reactions. The energy band structure of transition metal oxides can be represented as an orbital overlap between the transition metal d-orbitals and the oxygen p-orbitals, resulting in the formation of (M-O) and (M-O)* anti-bonds with strong ligand and metal characteristics, respectively. The oxygen's 1s-orbitals with lower energies are not redox-active and do not participate in bond formation, as shown in **Figure 7a-c**. In typical layered oxide materials, electrons lost due to redox reactions during the intercalation/de-intercalation of alkali metal ions are

first provided by (M-O)* anti-bonds. Once the electrons in the (M-O)* anti-bonds are consumed, additional electrons can only come from the stabilized (M-O) bonding bands (**Figure 7d**). **Figure 7e** shows that in the Li_2MO_3 Li-rich manganese-based structure, one of the O 2p orbitals (the one pointing to lithium in the $Li_{1/3}M_{2/3}O_2$ layer) is weakly bonded due to the relatively small overlap with the lithium 2s orbital. As a result, it behaves as an O non-bonded state, sometimes is referred to as an isolated or unhybridized O 2p state, or an O lone pair of electrons, or a Li-O-Li configuration, which is located between the (M-O) bond and the (M-O)* anti-bond. The material can provide additional electrons once the (M-O)* antibonding electrons are used up, leading to a two-band redox reaction and increased capacity[66]. The chemical formula for alkali metal-rich transition metal oxides is $A(A_\delta TM)O_2$, where δ and the number of lone pair electrons on each oxygen are related by $N_{LP} = 3\text{-}3(1\text{-}\delta) = 3\delta$[67].

In order to more accurately assess the energy band positions, it is first necessary to introduce the d-d Coulomb interaction term, which is used by solid state physicists to characterize on-site electron repulsion within d orbitals. This term favors localized electrons with opposite kinetic energies, leading to the splitting of the partially populated (M-O)* bands, also known as the Mott-Hubbard splitting. This splitting gives rise to the empty upper Hubbard band (UHB) and the filled lower Hubbard band (LHB), as shown in **Figure 7f**. The symbol Δ represents the charge transfer term, which indicates the energy difference between (M - O) and (M - O)*. The value of Δ is dependent on the electronegativity difference between M and O, denoted as Δχ. The value of U is inversely proportional to the orbital volume and is therefore strongly dependent on the d-metal involved. **Figure 7f-h** illustrate that the position of the LHB with respect to the O 2p nonbonding band depends on the relative values of U versus Δ, resulting in three different scenarios. In highly ionic oxides and fluorides with large M-L bonding energy (Δ), electrons are exchanged from the filled LHB[68,69], as shown in **Figure 7f**. When U/2 ≈ Δ, the LHB and O 2p non-bonding bands overlap, and both can participate in the electrochemical reaction, resulting in a double capacity, as shown in **Figure 7g**. This occurs sequentially in $Li_{2-x}RuO_3$ and simultaneously in $Li_{2-x}IrO_3$. To prevent unstable degenerate Fermi energy levels resulting from electron transfer, Jahn-Teller or Peierls distortion is used to lift the degeneration. This includes reorganizing the oxygen network and reducing symmetry to shorten O-O distances and allow for stabilizing $M\text{-}(O_2)^{n-}$ interactions. This method of stabilizing peroxo O-O-like dimers through covalent interactions of transition metals was previously referred to as "reductive coupling". Finally, **Figure 7h** shows that with U >> Δ, the single-band redox process remains present, but the electrons are now directly removed from the non-bonded O 2p band located above the filled LHB. Due to the high chemical hardness of the localized non-bonded O 2p states, the highly reactive O^{n-} may be delocalized from the metal-ion network by reductive elimination or attacking the electrolyte, leading to irreversible processes as observed in materials such as Li_2MnO_3[61].

The study of the origin of anionic activity has also received extensive attention. In $LiCoO_2$, the high covalency between Co and O atoms is typically considered to be the origin of the electronic structure of oxygen undergoing redox. In the low-spin state Co^{3+}, all six 3d electrons are typically located in the nonbonding t_{2g} (d_{xy}, d_{yz}, and d_{xz}) bands. Due to the high covalency of Co-O, the Co 3d state has a significant overlap with the O 2p state. Consequently, the electrons are initially removed from the Co t_{2g} state and participate in the redox process, which then triggers the oxygen redox when the Fermi energy levels are pinned to the top of the O 2p state during the subsequent delithiation process. The chemical and structural origin of oxygen redox in Li-rich layered oxides and cationic disordered oxides has been elucidated by Ceder and colleagues[70]. Their study identified that in lithium-excess or Li/M disordered oxides, the oxygen redox reaction predominantly occurs along the Li-O-Li configuration, generating unstable electrons from non-bonded oxygens. This arises from the inability of Li 1s to overlap with O 2p, which results in the formation of Li-O-Li, equivalent to O-non-bonded. In the ordered $LiMO_2$ structure, all the oxygen ions are coordinated to M ions, and there are no pure non-bonded O 2p states. However, as the average valence of M (which can be a combination of transition metals) increases, the Li-O-Li configuration will produce pure non-bonded O 2p states with high

energy. The oxidative reduction of oxygen in Li-rich oxides is primarily attributed to these pure non-bonded 2p states, rather than the σ-bonded states observed in the $LiMO_2$ case. As the Li/M ratio increases, the conformational Li-O-Li increases, resulting in a greater contribution to oxygen redox.

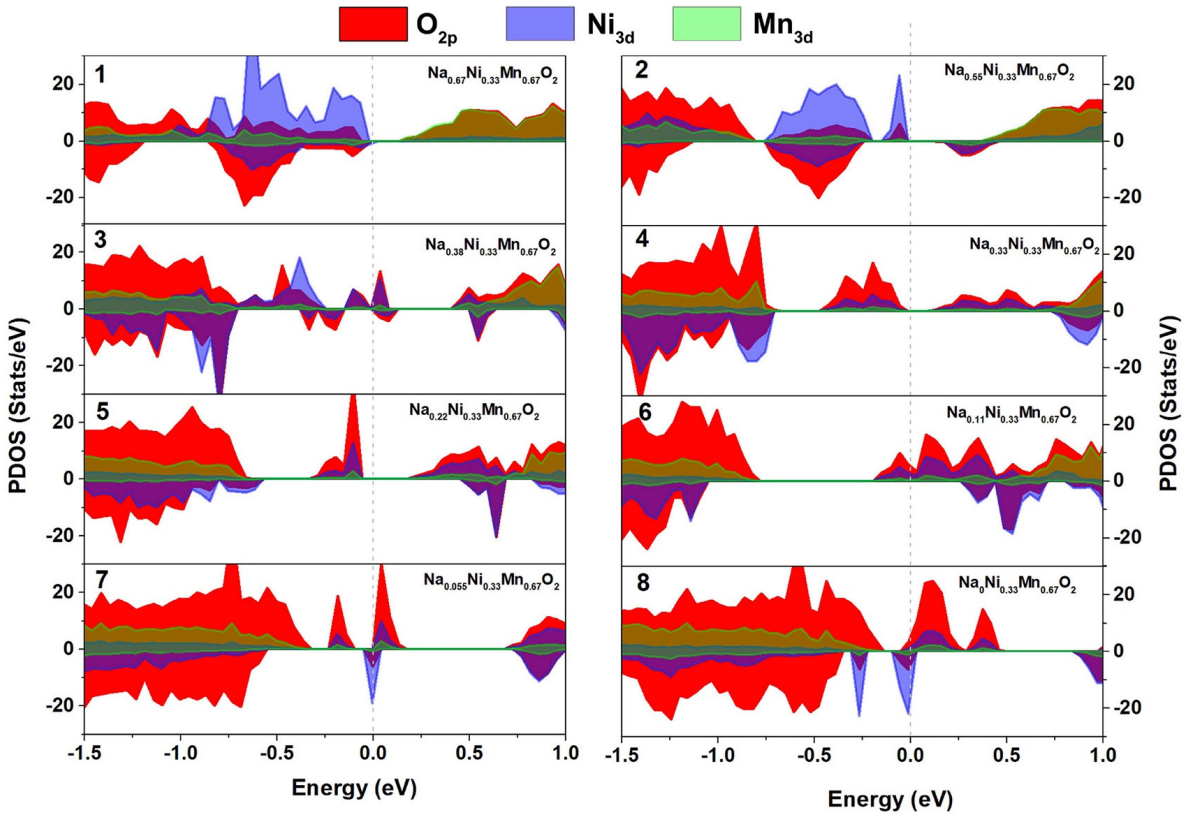

Fig 8. PDOS of $Na_xNi_{0.33}Mn_{0.67}O_2$ (x = 0.67, 0.55, 0.38, 0.33, 0.22, 0.11, 0.055, and 0). The states below and above zero (along y-axis) correspond to the electrons that spin-up and spin-down, respectively. Reproduced with permission[78]. Copyright 2020, Elsevier.

Considerable attention has been devoted to researching the redox of oxygen atoms in cathode materials for SIBs, leading to significant advancements. Firstly, a series of $Na_x(LiMn)O_2$ materials were prepared using lithium doping, such as $Na_{0.72}(Li_{0.24}Mn_{0.76})O_2$[71] and $Na_{0.6}(Li_{0.2}Mn_{0.8})O_2$[72]. Secondly, a series of $Na_x(MgMn)O_2$ materials were prepared using Mg doping, such as P2-type $Na_{2/3}Mg_{0.28}Mn_{0.72}O_2$[73], etc. Finally, a series of 4d transition metals were utilized as substrates to prepare Na_2RuO_3[74] and Na_2IrO_3[75]. The mentioned materials can explain the redox reaction of oxygen atoms based on non-bonded O 2p energy levels. However, post-transition metal layered oxides, such as $NaNi_{0.5}Fe_{0.5}O_2$[76] and $Na_{2/3}Ni_{1/3}Mn_{2/3}O_2$[77], do not have a non-bonding O 2p energy level, as shown by oxygen lone-pair calculations. Nevertheless, oxygen atom redox is still observed during the cycling process. Therefore, it can be concluded that the presence of oxygen lone pair electrons or non-bonded oxygen states is not a prerequisite for anion redox. As illustrated in **Figure 8**, density-functional theory(DFT) calculations were conducted for a representative P2-type $Na_xNi_{0.33}Mn_{0.67}O_2$ (x = 0.67, 0.55, 0.38, 0.33, 0.22, 0.11, 0.055, and 0), and the t_{2g} and e_g states of Mn are consistently distant from the Fermi energy level as Na is gradually de-intercalation, indicating that Mn^{4+} ions remain stable. When x equals 0.67 and 0.55, the valence band in close proximity to the Fermi energy level in $Na_xNi_{0.33}Mn_{0.67}O_2$ is predominantly influenced by the Ni 3d state. At x = 0.38, the partial densities of states (PDOS) of Ni and O are nearly identical, indicating that the charge of the de-intercalation Na ions is primarily compensated by the oxidation of the Ni ions during the period of x = 0.67-0.38. Furthermore, the probability of extracting electrons from the Ni ions and the lattice oxygen is similar at x =

0.38. Following further de-intercalation of Na^+, namely at x = 0.33, 0.22, and 0.11, the top valence band of $Na_xNi_{0.33}Mn_{0.67}O_2$ contributes predominantly to the O 2p state. This suggests that the charge compensation of sodium extraction via lattice oxygen oxidation, that is, after the Ni^{2+}/Ni^{3+} redox pair, is involved in lattice oxygen redox in $Na_xNi_{0.33}Mn_{0.67}O_2$. At very low sodium contents of x = 0.055 and 0, the top valence band of $Na_xNi_{0.33}Mn_{0.67}O_2$ is once again dominated by Ni 3d, suggesting that at the very end, the Ni^{3+}/Ni^{4+} redox pair provides charge compensation. In the most typical $Na_{0.67}Ni_{0.33}Mn_{0.67}O_2$ cathode material of P2-type Na_xTMO_2 compounds, Saubanère M et al.[65] employed X-ray absorption spectroscopy and DFT calculations to demonstrate that upon deintercalation of Na^+, Ni^{2+} was oxidized to Ni^{3+} and then the lattice oxygen was oxidized. DFT calculations further corroborated that the oxygen redox in $Na_{0.67}Ni_{0.33}Mn_{0.67}O_2$ originated from the Ni-O antibonding (e_g*) state rather than the non-bonding O 2p band. Further improvement of the oxygen atom oxidation reaction mechanism is needed for this class of materials.

Oxygen atom redox reactions can lead to materials with high discharge capacity, so materials with such reactions are considered one of the most promising cathode materials. However, their practical application is limited by certain challenges. The redox reaction may not always be reversible in all materials. When U >> Δ, the redox of this class of materials becomes irreversible, and the lattice oxygen precipitates irreversibly in the form of O_2. This leads to transition metal migration and structural damage. During the first charge-discharge process, the average discharge voltage decreases and the capacity decays due to several factors. These include the large voltage lag caused by the charge transfer band gap, asymmetric redox pair precipitation, the retarded nature of oxygen redox, and the ordering of alkali metal ions/transition metal ions in the transition metal layer[79]. To achieve practical application of the oxygen atom redox reaction, it is necessary to address the aforementioned challenges.

2.4 Migration and dissolution of transition metals

In the layered oxide cathode of LIBs, cation migration often occurs due to the similar ionic radii of Li and transition metals (TMs)[80]. In contrast, TMs in the layered cathodes of SIBs migrate to the Na layer, despite the large difference in ionic radii between Na and TMs. It is important to address this issue in the design of SIBs. This migration of TMs, especially Cr and Fe, has been reported most frequently and severely degrades the electrochemical performance[81]. Under high charging state, TMs irreversibly migrate to the Na layer, which reduces electrostatic repulsion between neighboring atoms in the TM layer. This narrows the spacing of the Na layer and hampers the diffusion of Na^+, resulting in decreased specific capacity of discharge and cycling stability[82]. To address this challenge, elemental doping can be used and the amount of migratable elements can be reduced.

The dissolution of transition metal ions is a common occurrence in LIBs and SIBs. This phenomenon is particularly prevalent in elements with Jahn-Teller effects, such as Mn^{3+} and Ni^{3+}[83]. Explain how the Jahn-Teller effect causes the dissolution of transition metal ions in acidic electrolytes through molecular orbital (MO) theory. The axial-equatorial splitting of the TM-O bond changes the degree of overlap between the atomic orbitals of the TM cation and O ligand. The e^1_g electronic configuration (e.g., $d^1_{z^2}$ $d^0_{x^2-y^2}$) allows the empty $d_{x^2-y^2}$ orbital to strongly overlap with the four filled 2p orbitals of the oxide ligand moiety in the equatorial x-y plane, yielding four predominantly oxygen s-bonded orbitals. However, the half-filled $d^1_{z^2}$ orbital, which is oriented along the z-axis, only weakly overlaps with the two filled 2p orbitals of the oxide ligand moiety along the same axis. This situation results in the creation of low-energy axial σ-bonding orbitals that are filled with oxide electrons and high-energy axial s-anti-bonding orbitals that are half-filled with d_{z^2} single electrons. The longer axial TM-O bonds with weaker overlap are more ionic than the shorter, more covalent equatorial TM-O bonds. This results in a higher negative charge on the axial oxygen atoms and stronger basicity from a Lewis acid-base perspective. The Jahn-Teller distortion increases reactivity with acids and TM-ionolysis in SIBs in two ways. Firstly, it puts an electron into the $d^1_{z^2}$ orbital, which is off-domain on the TM and O atoms. Secondly, it enhances the Lewis base strength of the axial oxygen compared to the equatorial oxygen. The hydrolysis of $NaPF_6$ salt in the electrolyte of a SIB produces a strong Lewis

acid, HF, due to residual moisture. The H^+ of the acid interact with the axial oxygen at the cathode-electrolyte interface, resulting in an acid-base interaction that leads to the formation of H_2O through oxide protonation. This process is accompanied by a simultaneous transfer of electrons from the metal to the ligand, which gives the TM a higher oxidation state. The TM cations formed, namely Mn^{4+}, Fe^{3+}, and Ni^{4+}, exhibit strong oxidizing properties that cause the electrolyte solvent molecules to oxidize into CO_2 and other reactive protonated species. These species are then directly reduced back to their stable forms without experiencing the Jahn-Teller effect, via a two-electron reduction pathway[84]. The resulting low-valent TM oxides and fluorides are stabilized and easily dissolve into the electrolyte. In turn, the water molecules formed can react with $NaPF_6$ salts to generate more HF, leading to the destruction of the electrolyte, anode, and cathode. To minimize the dissolution of transition metals, current modification strategies include surface capping, ion doping and defect introduction, and improvement of electrolyte high-pressure stability[85].

3. Modification Strategy for P2-Na_xTMO_2

3.1 Elemental doping

3.1.1 *Inactive single element doping*

Elemental doping is considered an effective strategy for improving the electrochemical performance of cathode materials. In their study, Chen et al.[86] prepared Li- and Mg-doped P2-$Na_{2/3}Ni_{1/3}Mn_{2/3}O_2$ sodium-ion cathode materials using co-precipitation and solid-phase sintering methods. The electrochemical properties of P2-$Na_{2/3}Ni_{1/3}Mn_{2/3}O_2$ varied significantly at different cutoff voltages. In the voltage range of 2.0-4.3 V, the first discharge capacity of P2-$Na_{2/3}Ni_{1/3}Mn_{2/3}O_2$ was 164.7 mAh g^{-1}. However, after 100 cycles, the capacity retention rate was only 27.6%. $Na_{2/3}Li_{0.1}Ni_{0.23}Mn_{0.67}O_2$ and $Na_{2/3}Mg_{0.1}Ni_{0.23}Mn_{0.67}O_2$ samples, which were doped with Li and Mg respectively, had capacities of 121.5 mAh g^{-1} and 114.6 mAh g^{-1}, respectively. The first discharge capacities of these samples were significantly reduced compared to the undoped samples. After 100 cycles, the capacity retention rates of $Na_{2/3}Li_{0.1}Ni_{0.23}Mn_{0.67}O_2$ and $Na_{2/3}Mg_{0.1}Ni_{0.23}Mn_{0.67}O_2$ were 79.9% and 89.7%, respectively. The cycling stability was significantly improved in both cases.

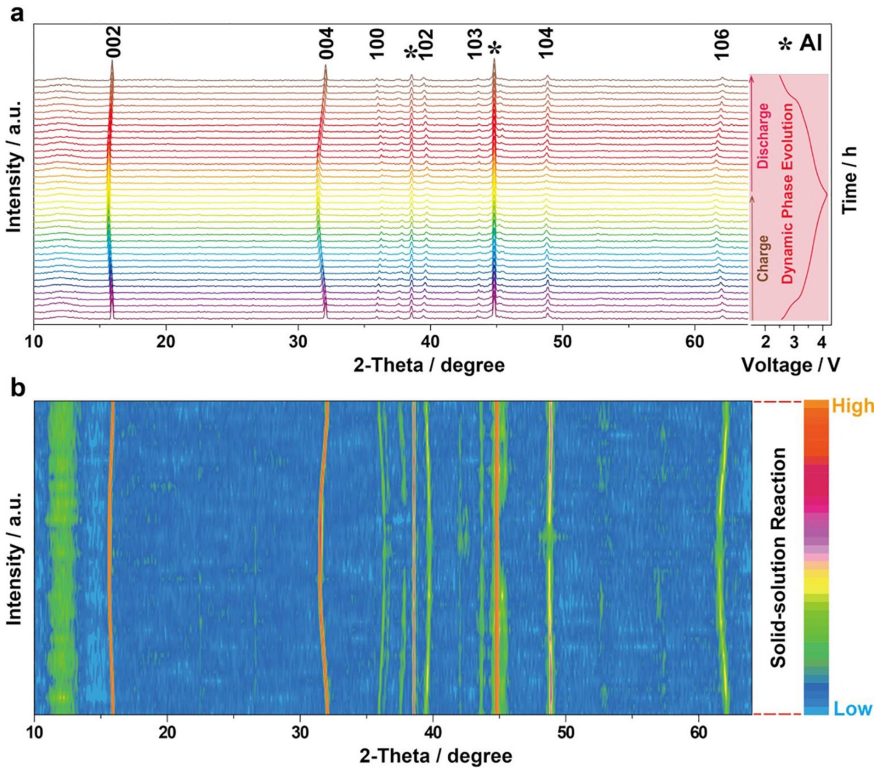

Fig 9. Crystal structure evolution of P2-NaLNM during Na^+ extraction/insertion. (a) in situ XRD patterns during charging/discharging at 0.1 C in the voltage range of 2.5-4.15 V. Black asterisks represent peaks from Al window. (b) corresponding intensity contour plots (bird's eye view) on the evolution of the main characteristic diffraction peaks. Reproduced with permission[87]. Copyright 2021, Elsevier.

The addition of Li^+ to the transition metal layer can result in a smoother charge/discharge curve, suppression of phase transition, and improved electrochemical performance. Li et al.[87] synthesized a multilayer of oriented stacked nanosheets of P2-$Na_{2/3}Li_{1/9}Ni_{2/9}Mn_{2/3}O_2$ cathode material. As shown in **Figure 9**, the (004) peak in the in-situ XRD maintained its shape throughout the charging and discharging process, indicating that the crystal structure remained in the P2 phase. This observation coincided with the smooth charging and discharging curves of P2-$Na_{2/3}Li_{1/9}Ni_{2/9}Mn_{2/3}O_2$ at 0.2 C, as well as within the voltage region of 2.5-4.15 V. These results suggest that the quasi-solid solution reaction transformed into a complete solid solution reaction during the charging and discharging process. The presence of monovalent Li^+ may cause an increase in the amount of Na^+ ions retained in the interlayer space to maintain overall charge balance. This can improve structural stability and delay high-voltage phase transitions, resulting in complete solid-solution reactions and smooth charge/discharge curves.

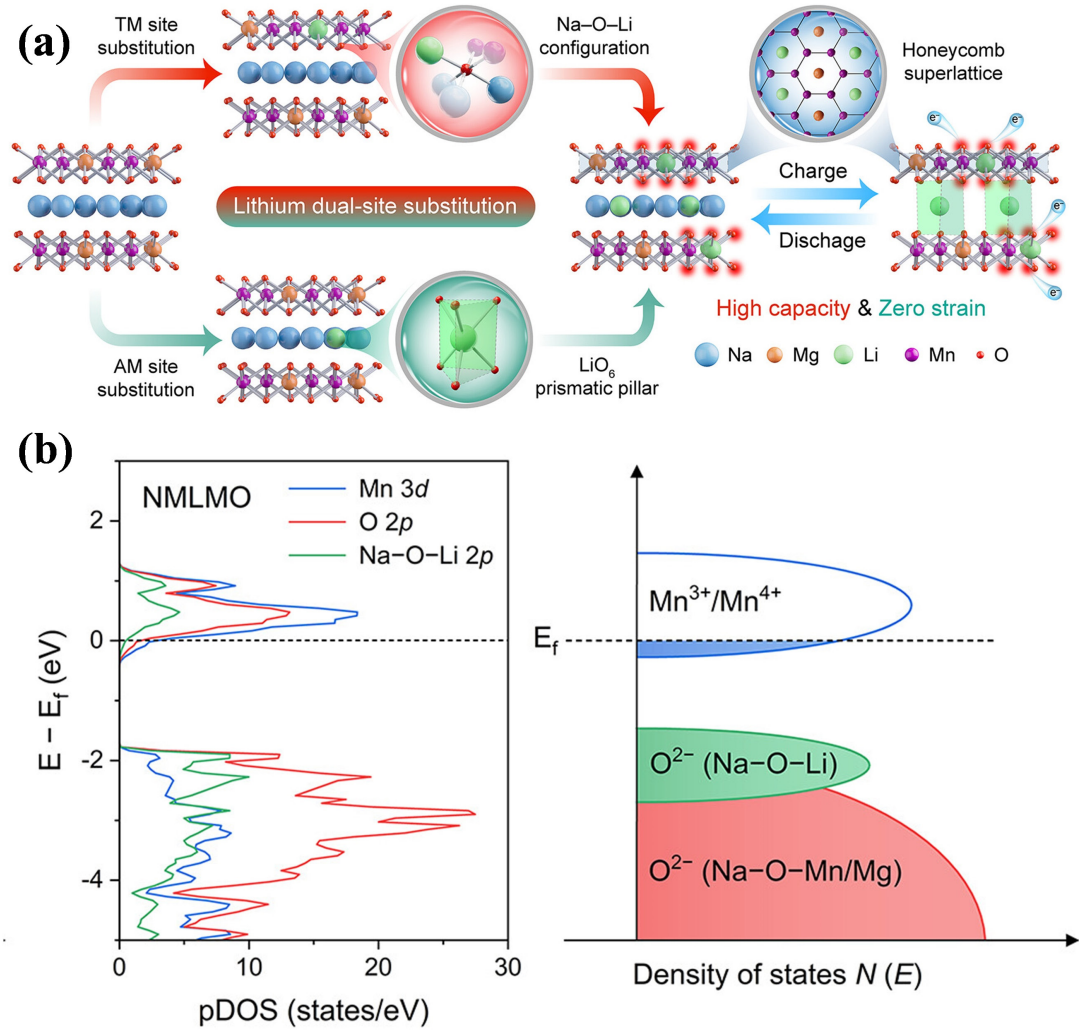

Fig 10. (a) Schematic of the mechanism of Li_{TM} and Li_{AM} to realize the high capacity and zero-strain characteristics of NMLMO. (b) calculated pDOS and schematic illustration of the energy vs DOS with the corresponding voltage for NMLMO. Reproduced with permission [88]. Copyright 2023, American Chemical Society.

Wu et al.[88] designed a cathode material with high capacity and zero-strain properties by substituting Li at two sites in P2-$Na_{0.7}Li_{0.03}[Mg_{0.15}Li_{0.07}Mn_{0.75}]O_2$(NMLMO). The roles of Li_{AM} and Li_{TM} in charge compensation and structural stability were investigated. As demonstrated in **Figure 10a**, the Li ion in the transition metal (TM) layer forms a Na-O-Li configuration. DFT calculations reveal the

presence of oxygen lone-pair electrons associated with the unbonded O 2p state in the electronic structure (**Figure 10b**), which can either contribute or receive additional charge during Na^+ (de)intercalation. Thus, the introduction of Li ions at the TM site not only facilitates the oxygen redox process but also enhances the specific capacity of NMLMO. Meanwhile, the lithium ions in the anode material layer act as prisms with a LiO_6 structure to suppress the phase transition and relieve the lattice strain. As a result, NMLMO has a lattice volume change of about 1.2 % during charging and discharging, while exhibiting a high specific capacity of 266 mAh g^{-1}.

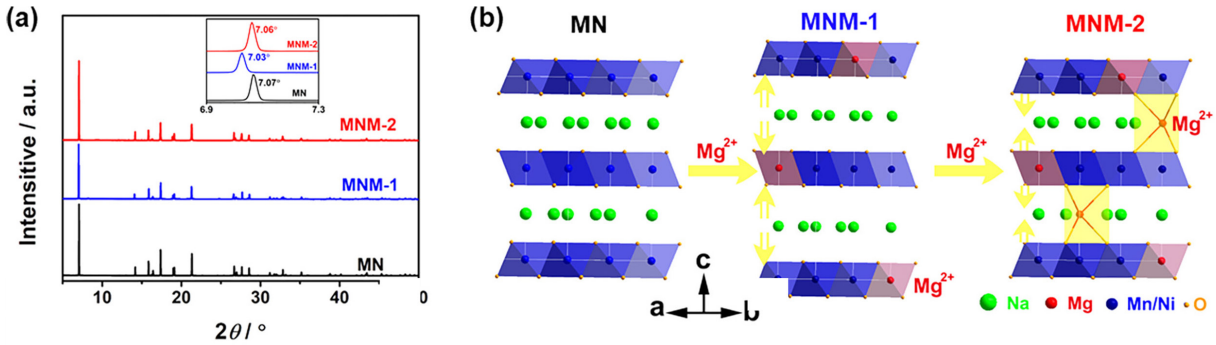

Fig 11. Structure of synthesized MNM-x. (a) XRD plots of synthesized MN, MNM-1 and MNM-2. Inset: Enlarged view of the (002) diffraction peak in the 2θ range from 6.9 to 7.3. (b) structural evolution of MNM-x with Mg substitution. Reproduced with permission[89]. Copyright 2019, American Chemical Society.

Wang et al.[89] synthesized a series of P2-$Na_{0.7}[Mn_{0.6}Ni_{0.4-x}Mg_x]O_2$ (x = 0, 0.1, and 0.2, denoted as MN, MNM-1, and MNM-2). This is the first time that Mg substitution at the Na site in P2 layered cathode materials for SIBs has been realized. The Na layer is doped with Mg ions to act as a "pillar" to inhibit structural collapse along the c-direction during high-voltage charging and to suppress the P2 → O2 phase transition. As shown in the **Figure 11a-b**, the XRD results indicate that their (002) diffraction peaks move linearly in the low 2θ direction as Mg increases from 0 to 0.2, and the cell expands along the c-axis when the Mg substitution is increased from x = 0 to x = 0.1, while the cell shrinks when Mg substitution is increased from x = 0.1 to x = 0.2. As the Mg substitution increases beyond x = 0.1, Mg^{2+} begin to occupy the Na site. The Mg^{2+} exhibit greater electrostatic attraction to the nearby oxygen layer due to their more positive charge than the Na^+. This leads to a decrease in c-axis interlayer spacing and an increase in structural stability. The prepared P2-$Na_{0.7}Ni_{0.2}Mn_{0.6}Mg_{0.2}O_2$ demonstrates excellent cycling stability, with 79 % capacity retention after 1000 cycles at 1 C.

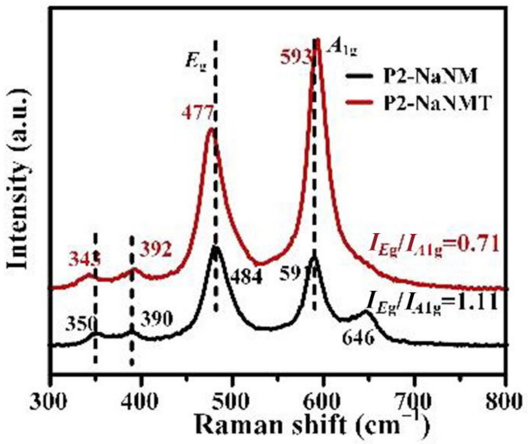

Fig 12. Raman spectra of P2-NaNM and P2-NaNMT. Reproduced with permission[90]. Copyright 2021, Elsevier.

Zhong et al.[90] synthesized P2-$Na_{2/3}Ni_{1/3}Mn_{2/3}O_2$ and P2-$Na_{2/3}Ni_{1/3}Mn_{1/3}Ti_{1/3}O_2$ using the high-temperature solid-phase method. They monitored the chemical changes during charging and discharging through in situ Raman spectroscopy of P2-$Na_{2/3}Ni_{1/3}Mn_{1/3}Ti_{1/3}O_2$ and P2-$Na_{2/3}Ni_{1/3}Mn_{2/3}O_2$. As shown in **Figure 12**, after Ti partially replaces Mn, the A_{1g} peak is blue-shifted, indicating compression of the transition metal layer TMO_6, and the E_g peak is red-shifted, indicating an increase in the cell paramatera. Ti substitution leads to compression of the transition metal layer and expansion of the planar oxygen layer in the cell, stabilizing the structure of the P2 phase and improving the cycling stability of P2-$Na_{2/3}Ni_{1/3}Mn_{1/3}Ti_{1/3}O_2$.

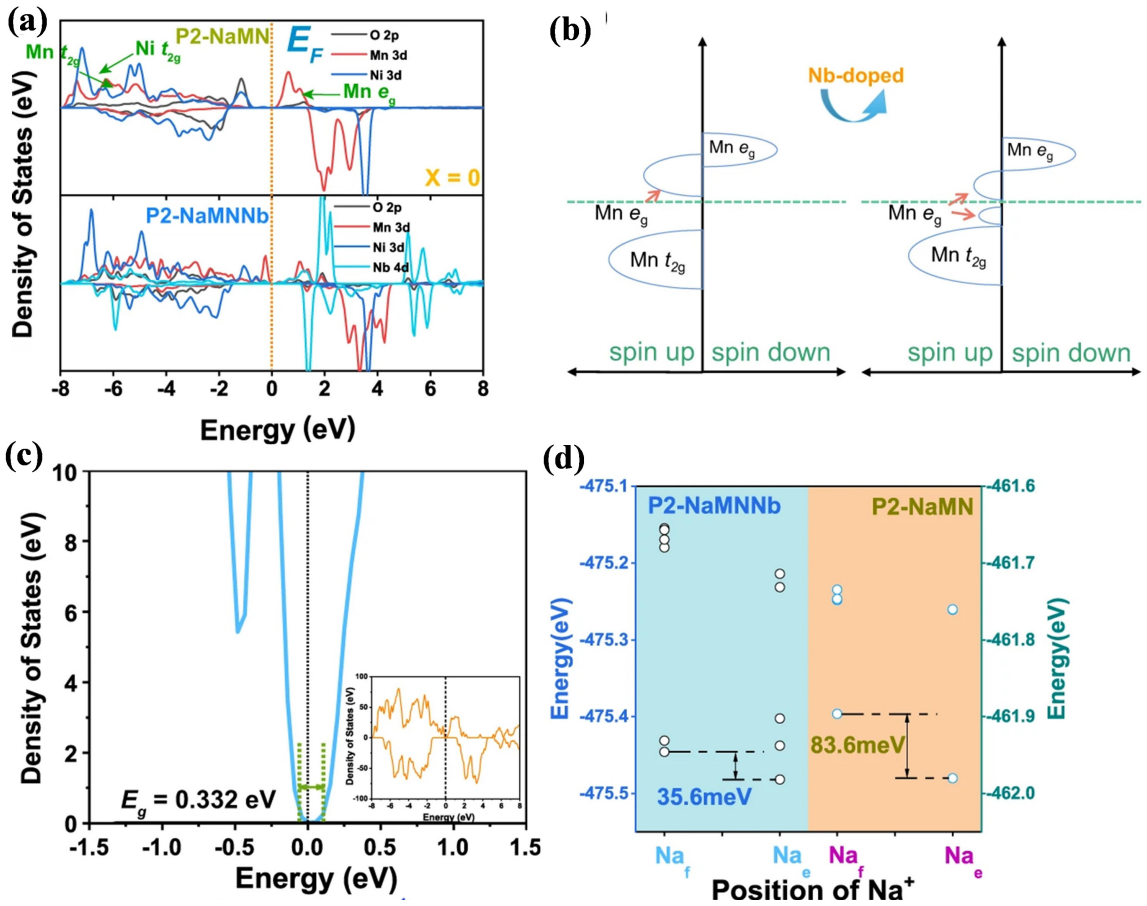

Fig 13. (a) partial density of states (pDOS) of O 2p, Mn 3d, and Ni 3d and Nb 4d orbitals with x = 0. (b) schematic pDOS of P2-NaMN and P2-NaMNNb with x = 0. (c) the total density of state of $Na_{24}Ni_9Mn_{22}Nb_1O_{64}$. (d) calculated energy difference between the Na_e and Na_f site for P2-NaMNNb (blue background) and P2-NaMN (orange background). Reproduced with permission[91]. Copyright 2021, Qinhao Shi.

Shi et al.[91] proposed a P2-$Na_{0.78}Ni_{0.31}Mn_{0.67}Nb_{0.02}O_2$ (P2-NaMNNb) anode active material. DFT calculations showed that niobium doping reduces the electronic bandgap and increases the electronic conductivity. As shown in **Figure 13a-c**, after Nb doping, the Mn e_g orbital splits into two peaks, and one of the peaks moves below the Fermi energy level to maintain charge conservation, and the bandgap (e_g) is reduced from 0.500 eV to 0.332 eV, which improves the electronic conductivity. In **Figure 13d**, the energy difference between the Na_e and Na_f sites of $Na_{0.78}Ni_{0.31}Mn_{0.67}Nb_{0.02}O_2$ is reduced from 83.6 to 35.6 meV compared with that of the undoped $Na_{0.78}Ni_{0.32}Mn_{0.68}O_2$, lowering the ion diffusion energy barrier in favor of increasing the mobility of sodium ions. At 25 °C under 9.2 A g^{-1} (50 C), it exhibited a discharge capacity of approximately 65 mAh g^{-1}. After undergoing 1800 cycles of charging and discharging at 368 mA g^{-1} and -40 °C, the battery maintained a capacity of approximately 76% and a final discharge

capacity of around 70 mAh g^{-1}.

3.1.2 *Reactive single element doping*

Doping inactive elements can enhance the cycling stability of the material, but it comes at the cost of losing some of the capacity since the transition metal elements that contribute to the capacity are partially replaced. On the other hand, doping active elements has a dual advantage of improving the cycling stability of the material while minimizing the loss of capacity.

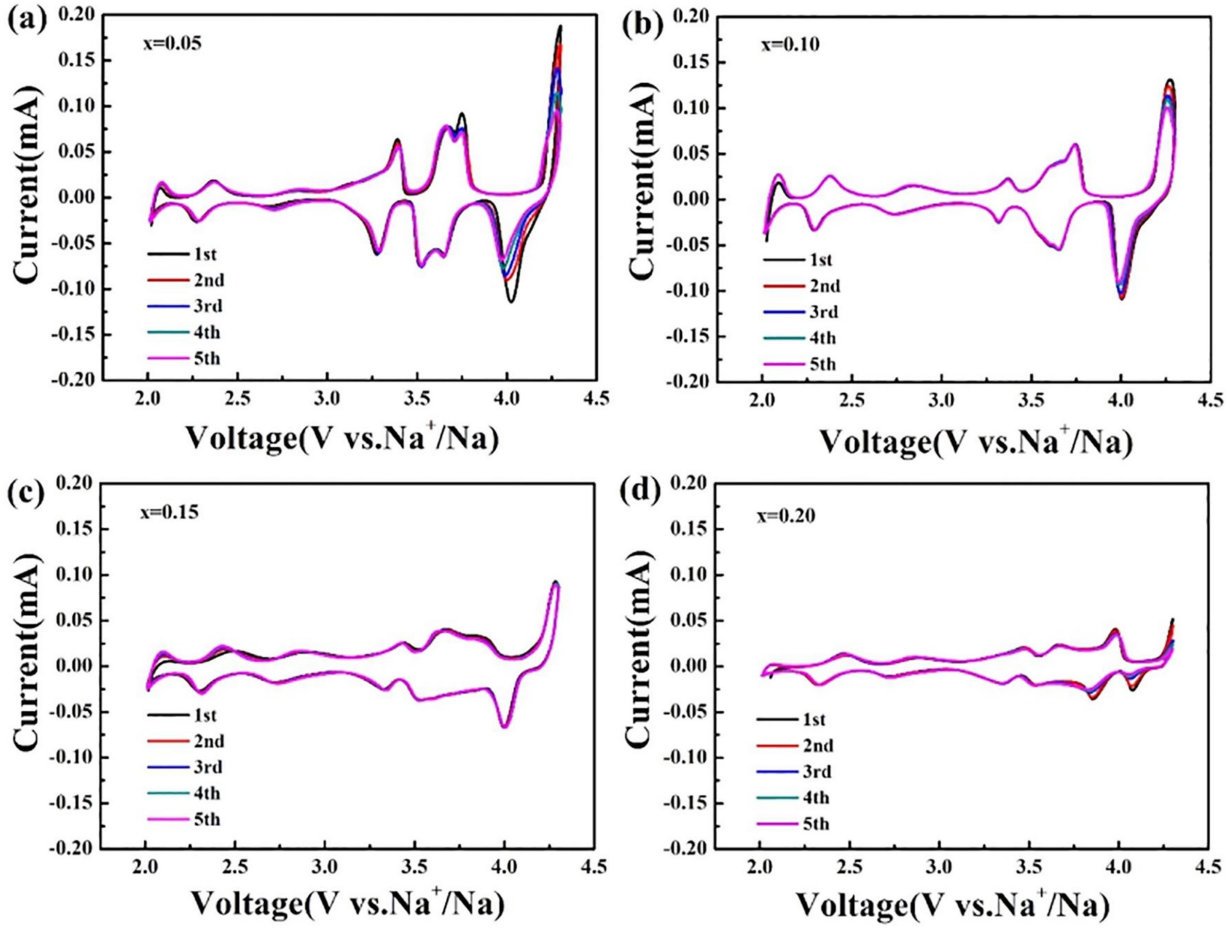

Fig 14. CV curves of NNCM measured at 0.1 mV s^{-1} within the voltage range 2-4.3 V. (a) x = 0.05. (b) x = 0.10. (c) x = 0.15. (d) x = 0.20. Reproduced with permission[92]. Copyright 2021, Elsevier.

Yang et al.[92] prepared a series of Cu-doped layered P2-$Na_{0.67}Ni_{0.33-x}Cu_xMn_{0.67}O_2$ (x = 0, 0.05, 0.10, 0.15, 0.20, 0.33) using a solid-phase method. The introduction of electrochemically active Cu^{2+} ions as substituents improved capacity retention, cycling stability, and rate capability. **Figure 14a-d** shows that the degree of overlap of the CV curves increased gradually with increasing doping up to x = 0.15. When x = 0.15, the initial five cycles of the CV curves were almost completely overlapped, indicating excellent reversibility and cycling stability. However, when the doping level was increased to x = 0.2, the consistency of the CV curves deteriorated, and the overdoping worsened the cyclic reversibility. At x = 0.15, the samples exhibited a first discharge capacity of 120 mAh g^{-1} at 0.1 C within the voltage range of 2-4.3 V. After 200 cycles, the capacity retention was 78%, and the reversible capacity was 62 mAh g^{-1} at 20 C. The improved electrochemical performance, compared to the pristine compounds, can be attributed to the insertion of Cu^{2+} into the transition metal (TM) layer. This insertion stabilizes the P2 phase structure and prevents the P2-O2 phase transition during charging to high voltages. The reversible capacity is also influenced by the presence of copper due to the Cu^{2+}/Cu^{3+} redox reaction.

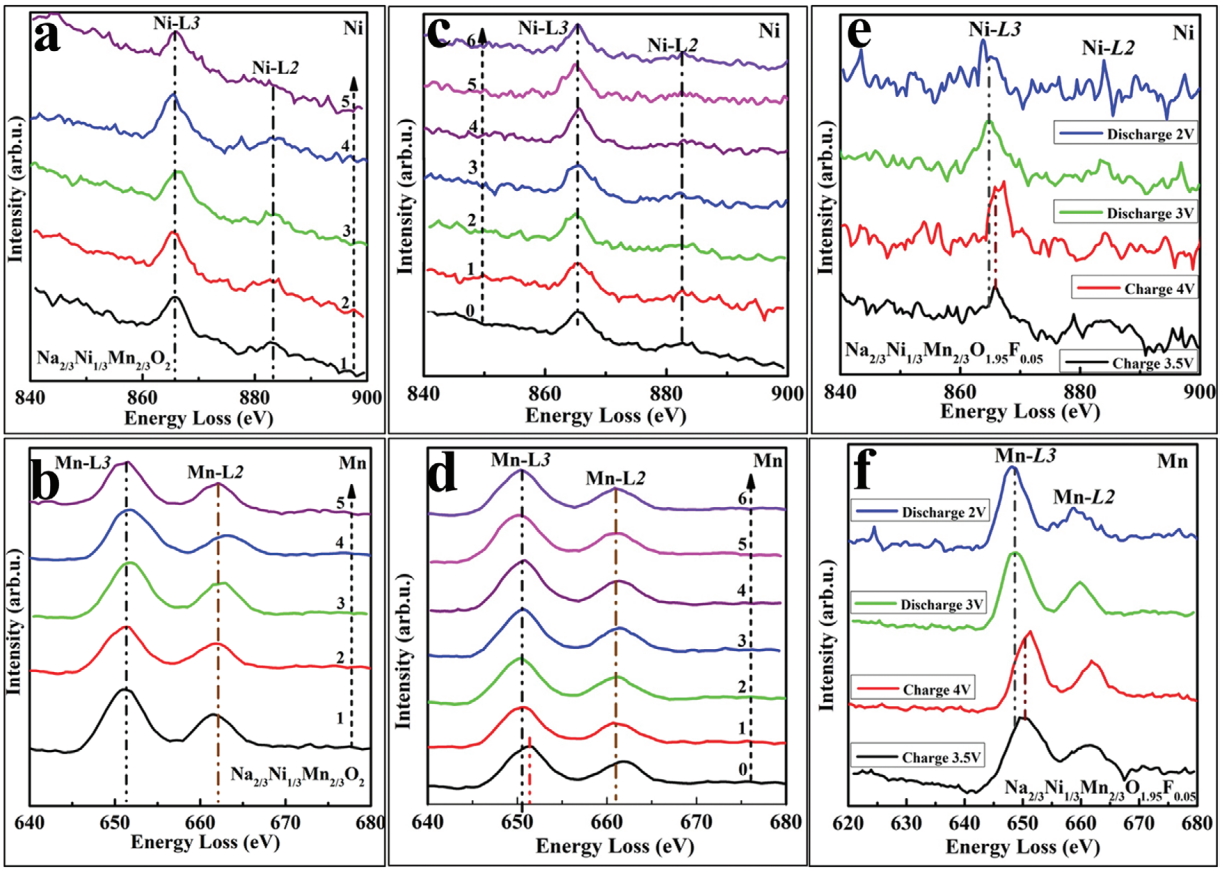

Fig 15. EELS spectra of $Na_{2/3}Ni_{1/3}Mn_{2/3}O_2$ from surface (point 1) to interior (point 5). (a) Ni L-edge signals. (b) Mn L-edge signals. EELS spectra of $Na_{2/3}Ni_{1/3}Mn_{2/3}O_{1.95}F_{0.05}$ from surface (point 1) to interior (point 6). (c) Ni L-edge signals. (d) Mn L-edge signals. EELS spectra of $Na_{2/3}Ni_{1/3}Mn_{2/3}O_{1.95}F_{0.05}$ during Na^+ extraction/insertion process. (e) Ni L-edge signals. (f) Mn L-edge signals. Reproduced with permission[93]. Copyright 2020, Wiley.

Anion doping is regarded as a promising approach to enhance the specific capacity and cycling stability of cathode materials. It is generally believed that the substitution of F for O enables the partial reduction of Mn^{4+} to Mn^{3+}, thus improving the cycling stability[94]. Chen et al.[95] reported that the improvement in capacity and rate performance was caused by the reduction of the Ni^{2+}/Ni^{3+} ratio under fluorination. Liu et al.[93] synthesized a series of F-substituted $Na_{2/3}Ni_{1/3}Mn_{2/3}O_{2-x}F_x$ (x = 0, 0.03, 0.05, 0.07) anode materials. The incorporation of F into the bulk crystal structure was confirmed by solid-state nuclear magnetic resonance (ssNMR), cross-sectional scanning transmission electron microscopy, and X-ray photoelectron spectroscopy (XPS). As illustrated in **Figure 15a-b**, the Ni L-edge and Mn L-edge spectra of $Na_{2/3}Ni_{1/3}Mn_{2/3}O_2$ from the surface (point 1) to the interior (point 5) exhibit nearly identical characteristics, thereby confirming that the valence states of Ni and Mn remain consistent from point 1 to point 5, respectively. This also indicates that the synthesized material maintains the coherent texture belonging to the P2-type layered structure. **Figure 15c** illustrates the Ni L edge spectra of $Na_{2/3}Ni_{1/3}Mn_{2/3}O_{1.95}F_{0.05}$ from the surface (point 1) to the interior (point 6). The pristine $Na_{2/3}Ni_{1/3}Mn_{2/3}O_2$ is used as a reference and designated as point 0. All the selected points show almost the same spectra, indicating that the Ni ions are not involved in the charge compensation process. However, the Mn L-edge spectra of $Na_{2/3}Ni_{1/3}Mn_{2/3}O_{1.95}F_{0.05}$, as shown in **Figure 15d**, exhibit a notable shift relative to the Mn L-edge spectra of $Na_{2/3}Ni_{1/3}Mn_{2/3}O_2$ (point 0). This shift is observed for both Mn L3 and Mn L2, with the values changing from 650 to 652 eV and from 661 to 662 eV, respectively. This confirms the reduction in the oxidation state of Mn ions after fluorination. Concurrently, the peak positions of the Mn L-edge spectra of $Na_{2/3}Ni_{1/3}Mn_{2/3}O_{1.95}F_{0.05}$ remained constant from point 1 to point 6, indicating coherent

reduction of Mn ions by uniform F-substitution from the surface to the interior of the particles in order to maintain electroneutrality. **Figure 15e** illustrates the apparent changes in the Ni L-edge spectra under different voltage conditions, suggesting that the Ni^{2+}/Ni^{3+} redox pair is primarily responsible for charge compensation during cycling, as previously reported. Interestingly, the Mn L2,3-edge spectra also exhibited a significant shift during charging and discharging (**Figure 15f**), indicating for the first time that the Mn^{3+}/Mn^{4+} redox pair is also involved in the charge compensation process during cycling[96]. The absorption near-edge structure (XANES) revealed the potential charge compensation mechanism, namely that fluorine substitution induces the partial reduction of Mn^{4+} to Mn^{3+} through electroneutrality, which changes the single redox center of Ni^{2+} and promotes the increase of the specific capacity of SIBs. The structural changes occurring during the charging and discharging processes were revealed by in situ XRD, which demonstrated that the F-substitution significantly inhibited the biphasic reaction in the low-voltage region. The $Na_{2/3}Ni_{1/3}Mn_{2/3}O_{1.95}F_{0.05}$ sample provided an ultra-high specific capacity of 61 mAh g^{-1} after 2,000 cycles at 10 C and 30℃, extraordinary cycling stability with 75.6% capacity retention after 2,000 cycles at 10 C and 55 ℃, and excellent full cell performance with 89.5% capacity retention after 300 cycles at 1 C.

3.1.3 *Two element doping*

Bi-elemental doping can leverage the synergistic effect of two elements to achieve superior modification.

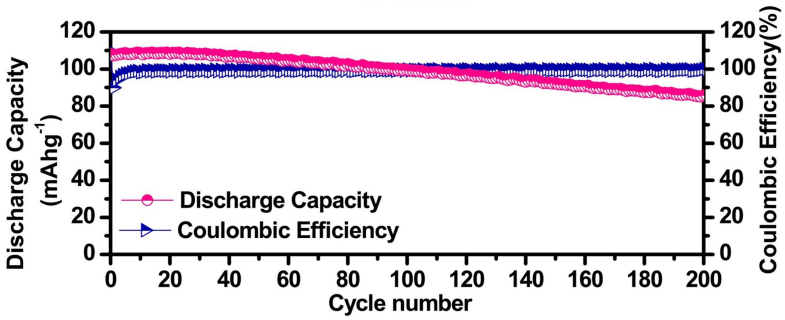

Fig 16. Cyclic performance of NLCMO-2 at the rate of 0.2 C in the potential window of 2.0-4.2 V. Reproduced with permission [97]. Copyright 2023, Elsevier.

Anilkumar et al.[97] successfully synthesized Li and Cu double doped $Na_{0.85}Li_{0.05}Cu_{0.05}Ni_{0.3}Mn_{0.6}O_2$ (NLCMO-1) $Na_{0.93}Li_{0.07}Cu_{0.07}Ni_{0.29}Mn_{0.57}O_2$ (NLCMO-2) and $Na_{0.9}Li_{0.1}Cu_{0.1}Ni_{0.2}Mn_{0.6}O_2$ (NLCMO-3) cathode materials by using sol-gel method. The co-doping of Li and Cu has a synergistic effect that effectively inhibits the Na^+/vacancy order and the P2 - O2 phase transition, resulting in improved capacity and structural stability. The cathode $Na_{0.93}Li_{0.07}Cu_{0.07}Ni_{0.29}Mn_{0.57}O_2$ exhibits a first discharge capacity of 110 mAh g^{-1} within the voltage range of 2.0-4.2 V at 0.2 C. After 200 cycles, the capacity retention rate is approximately 85% (**Figure 16**).

Chen et al.[98] synthesized four different cathode materials: $Na_{0.67}Ni_{0.33}Mn_{0.67}O_2$ (NNMO), $Na_{0.67}Ni_{0.32}Mn_{0.59}Ti_{0.08}O_2$ (NNMTO), $Na_{0.67}Ni_{0.25}Zn_{0.08}Mn_{0.67}O_2$ (NNZMO), and $Na_{0.67}Ni_{0.29}Zn_{0.04}Mn_{0.63}Ti_{0.04}O_2$ (NNZMTO). Ti doping with similar ionic radii and different Fermi energy levels as the main Mn atoms can disrupt the Na^+/vacancy ordering and effectively suppress the Jahn-Teller aberration and lattice oxygen loss. Additionally, introduced Zn atoms can induce localized Na-O-Zn configurations, buffer the interlayer O^{2-} - O^{2-} electrostatic repulsion, promote reversible anion redox, and fundamentally inhibit unfavorable phase transition and O_2 release. $Na_{0.67}Ni_{0.29}Zn_{0.04}Mn_{0.63}Ti_{0.04}O_2$ material co-doped with Ti and Zn has a capacity retention of 67 % after 300 cycles at 0.5 C.

Kong et al.[99] prepared a series of anode materials, including P2-type $Na_{0.67}Mn_{0.75}Ni_{0.25}O_2$ (bare), $Na_{0.67}Mn_{0.71}Cu_{0.04}Ni_{0.25}O_2$ ($Cu_{0.04}$), $Na_{0.67}Mn_{0.71}Mg_{0.04}Ni_{0.25}O_2$ ($Mg_{0.04}$), and $Na_{0.67}Mn_{0.71}Cu_{0.02}Mg_{0.02}Ni_{0.25}O_2$ ($Cu_{0.02}Mg_{0.02}$). As shown in **Figure 17a-b**, the Mn^{3+} / Mn^{4+} ratios of bare, $Cu_{0.04}$, $Mg_{0.04}$ and $Cu_{0.02}Mg_{0.02}$ are 0.471,0.419,0.363 and 0.313, respectively. With the substitution of Cu and Mg, the relative content of Mn^{3+} decreases, and the ratio of $Cu_{0.02}Mg_{0.02}$ with Cu-Mg co-doping synergistic effect

decreases the most. The reduction of Mn^{3+}/Mn^{4+} in $Cu_{0.02}Mg_{0.02}$ cathode materials is advantageous in inhibiting Jahn-Teller distortion and enhancing the stability of the laminar structure. The highest relative content of lattice oxygen is found in $Cu_{0.02}Mg_{0.02}$ cathode materials (**Figure 17c-d**), and the most stable laminar structure is achieved through the strongest binding energy between transition metals and oxygen. In addition, co-doping with Cu and Mg has several benefits. Firstly, it enlarges the d-spacing, which helps to alleviate the Na^+ diffusion barrier and improves the Na^+ diffusion coefficient. Secondly, it reduces the TM-O length and enhances the TM-O bonding energy, which improves the oxygen redox reversibility and the stability of the layered structure. Thirdly, it raises the thermal decomposition temperature and the reversible transition from the P2 phase to the O2 phase, further enhancing the anion redox reversibility. As a result, the battery exhibits excellent cycling stability.

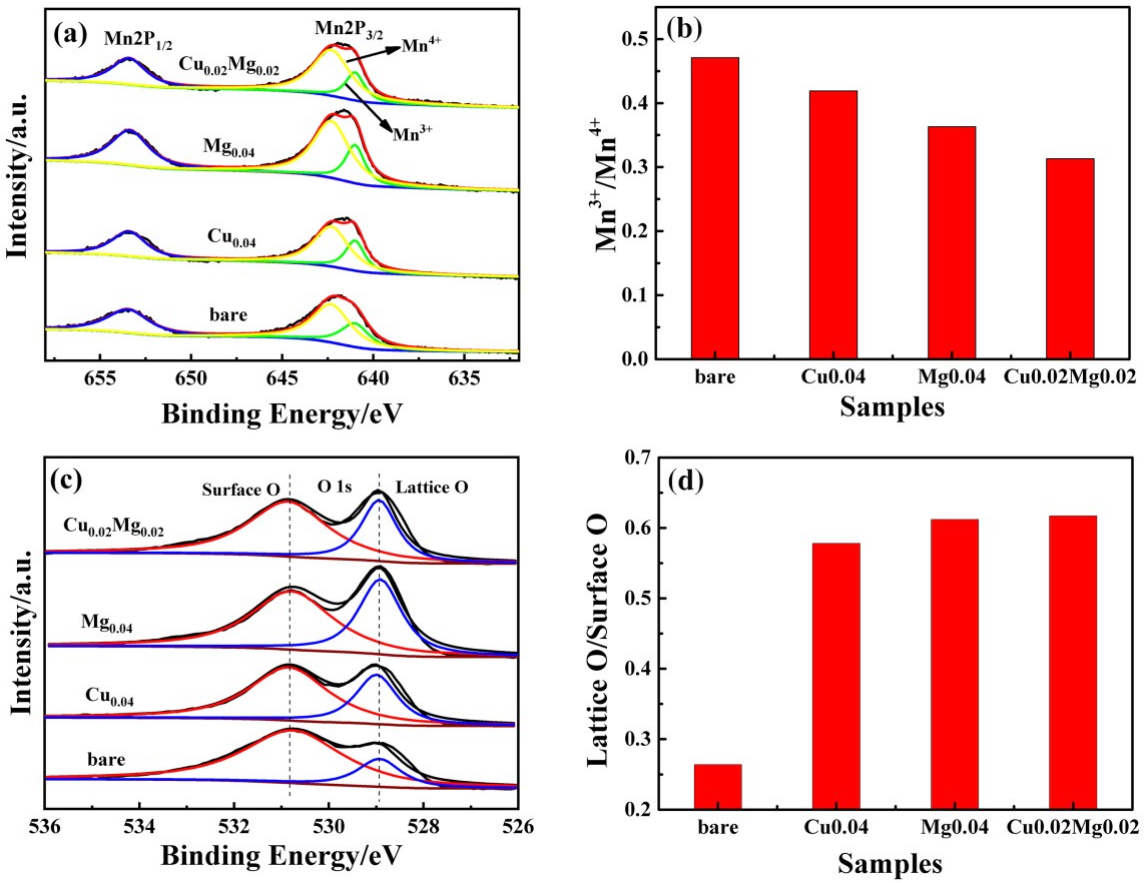

Fig 17. XPS spectra of the cathode samples: (a) Mn. (b) the ratio of Mn^{3+}/Mn^{4+}. (c) O. (d) the ratio of lattice oxygen/surface oxygen. Reproduced with permission[99]. Copyright 2019, Royal Society of Chemistry.

Previous reports have indicated that a number of elemental doping strategies are available for the purpose of enhancing the electrochemical performance. The electrochemical properties of layered oxides can be optimised by a variety of ion doping strategies. It has been demonstrated that ion doping strategies typically alter the local chemistry, electronic structure, and phase transitions during the intercalation/de- intercalation process, thereby improving the performance. The incorporation of various elements into layered oxides modifies the local chemistry, electronic structure, and phase transitions during the intercalation/de-intercalation processes, thereby enhancing their properties. Nevertheless, although phase transitions are suppressed at certain contents, lattice changes and intracrystalline crack generation are unavoidable during long-term cycling, which ultimately leads to unsatisfactory cycle life. In addition, the atomic weight,

interactions, and electrochemical activities of different doping elements vary, necessitating a rational design and skillful application[100].

3.2 P2/O3 biphasic modification

In recent years, some researchers have combined the advantages of the high rate performance of P2-type materials and the high theoretical specific capacity of O3-type materials to utilize the P2/O3 biphasic synergism to further improve the electrochemical properties of the materials.

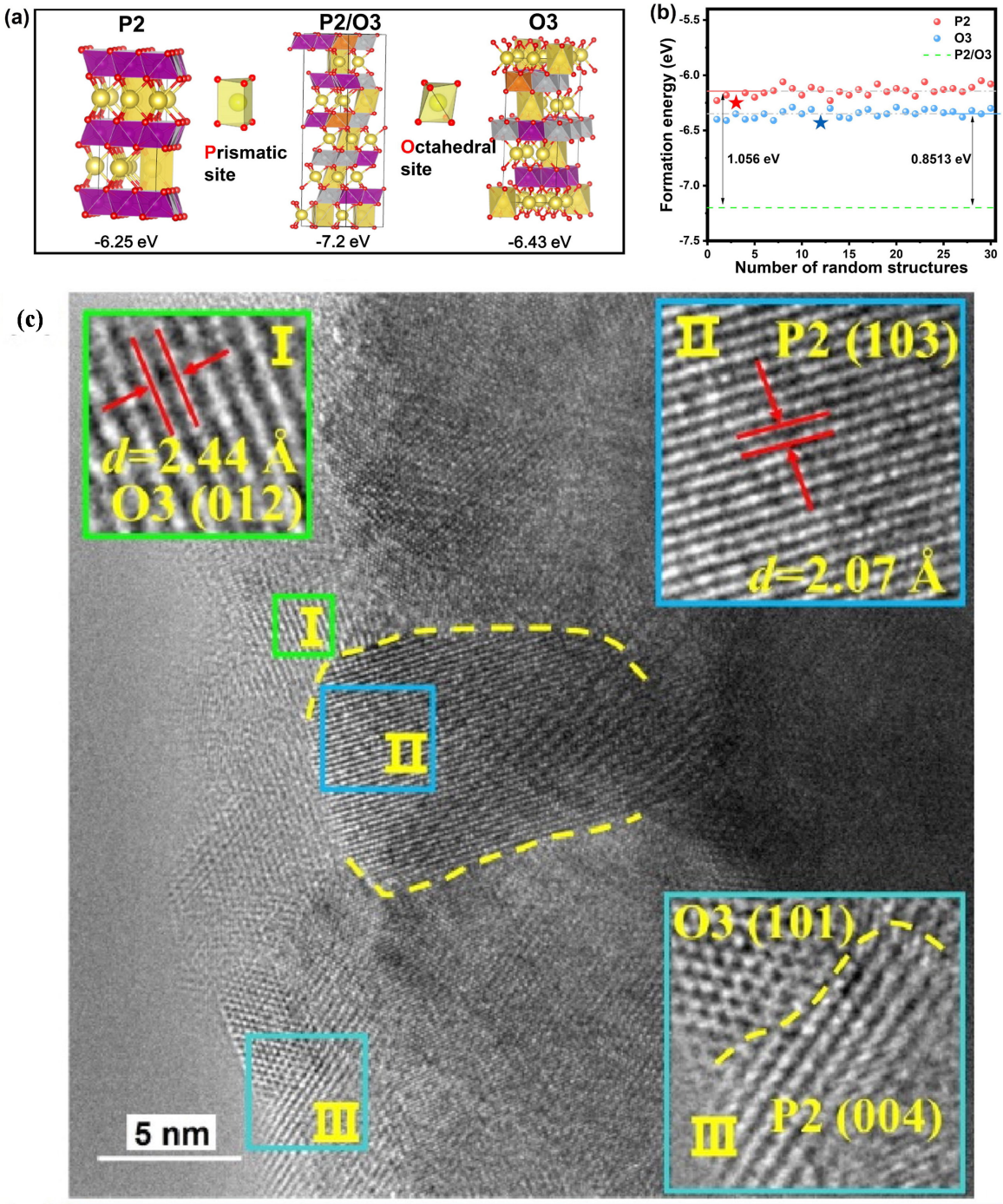

Fig 18. (a) crystal structure diagrams and E_f of $Na_{0.736}Ni_{0.264}Mg_{0.1}Mn_{0.636}O_2$ when it formed P2 phase, O3 phase, and P2/O3 biphase structure at the lowest energy, respectively. (b) comparison of E_f between the single and P2/O3 biphase structure. (c) TEM images of P2/O3-Com_{950} 0.8 materials with the insert of SEAD image and partly enlarged graphic. Reproduced with permission[101]. Copyright 2023, Elsevier.

Zhang et al.[101] employed a co-precipitation method to synthesize precursors of $Na_{0.67}Ni_{0.23}Mg_{0.1}Mn_{0.67}O_2$ ($Na_{0.67}$-NMMO), $NaNi_{0.4}Mg_{0.1}Mn_{0.5}O_2$ (Na-NMMO), and P2/O3-composites. P2/O3-composite materials were rationally designed based on the ratio of Na0.67-NMMO and Na-NMMO with 4:1, 2:1, 1:1, and 1:2. These materials were named as P2/O3-Com 0.8, P2/O3-Com 0.67, P2/O3-Com 0.5, and P2/O3-Com 0.33, respectively, based on the rational ratio of the P2 phase. DFT calculations indicate that the lowest formation energy (E_f) corresponds to the formation of a two-phase structure in $Na_{0.736}Ni_{0.264}Mg_{0.1}Mn_{0.636}O_2$. This suggests that a two-phase structure is most likely to form in this material (**Figure 18a-b**). The lattice stripes on both sides of the dislocation line in insertion region III correspond to the (101) face of the O3 phase and the (004) face of the P2 phase, respectively (**Figure 18c**). Therefore, the P2/O3 phase does not grow as isolated individual particles in the P2/O3-Com_{950} 0.8 material, but forms symbiotic structures on the atomic scale. The P2 and O3 phases have a symbiotic structure that may result in interlocking effects. This symbiosis is considered a heterogeneous epitaxial-like structure with multiphase boundaries that are shared. During the charging and discharging process, the TMO_2 plate of one phase slides, while the neighboring TMO_2 plate of the other phase remains stationary or slides in the opposite direction. The adjacent TMO_2 layers provide a supporting force that prevents sliding behavior and mitigates lattice strain induced by Na^+ detachment/intercalation. The symbiotic P2/O3 composites with interlocking effect exhibit excellent structural reversibility and long cycle stability. One of the materials, $Na_{0.732}Ni_{0.273}Mg_{0.096}Mn_{0.63}O_2$, is biphasic and consists of 78.39 wt% P2 phase and 21.61 wt% O3 phase. This material has a specific capacity of 130 mAh g^{-1} at 0.1 C and a capacity retention of 73.1% after 200 cycles at 1 C.

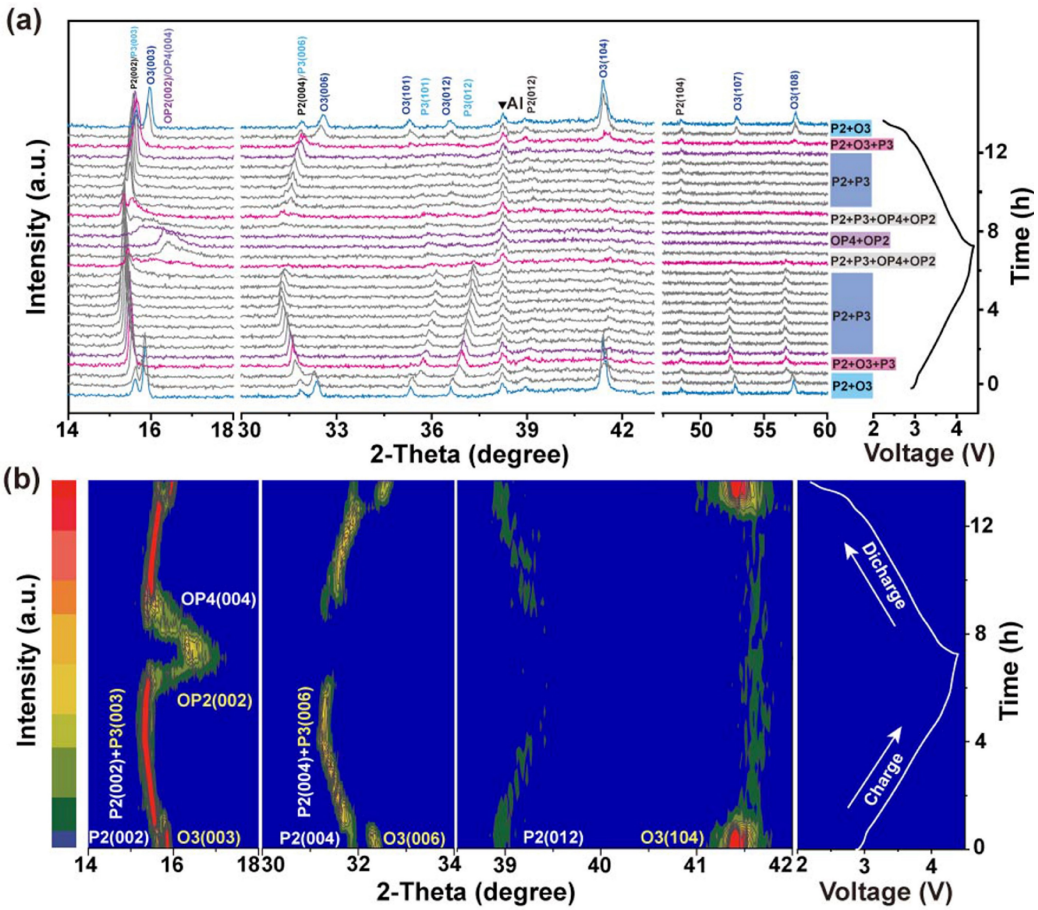

Fig 19. (a) operando XRD patterns of P2/O3-NMT_3 during the first charge/discharge at 0.1 C in the voltage range of 2.2-4.4 V. (b) corresponding intensity contour maps concerning the evolution of the main characteristic diffraction peaks. Reproduced with permission.[102]. Copyright 2022, Elsevier.

Yu et al.[102] prepared a series of $Na_{0.85}Ni_{0.34}Mn_{0.66-x}Ti_xO_2$ (x = 0, 0.11, 0.22, 0.33, 0.44, denoted NM, NMT_1, NMT_2, NMT_3, and NMT_4, respectively) cathode materials by the conventional high-temperature solid-phase method. NM is a pure P2 phase, while NMT_1, NMT_2, and NMT_3 are P2/O3 two-phase hybrids, and NMT_4 is a pure O3 phase. **Figure 19a-b** shows that the P2/O3-NMT_3 material did not exhibit the O2 phase or the diffraction peaks of O3' during the charging and discharging process, indicating that the P2-O2 and O3-O3' phase transitions that typically occur during charging to high voltages were suppressed. The material underwent P2/O3-P2/P3-OP4/OP2-P2/P3-P2/O3 structural evolution during cycling, with good structural reversibility. The biphasic P2/O3-$Na_{0.85}Ni_{0.34}Mn_{0.33}Ti_{0.33}O_2$ anode demonstrated an outstanding capacity retention of 80.6% after 200 cycles at 1 C. Additionally, the full cell, which was assembled with a hard carbon anode, achieved a high energy density of 294.6 Wh kg^{-1}.

The development of P2/O3 biphasic cathode materials with a synergistic effect represents a promising avenue for achieving comprehensive sodium storage performance. By combining the characteristics of the P2 phase, which exhibits a stable structure and rapid Na^+ migration, with those of the O3 phase, which contains a high sodium content, it is possible to circumvent the limitations associated with the P2 phase, including its low Coulombic efficiency due to the lack of sodium and the slow kinetics of the O3 phase, which are a consequence of its complex phase transition. The electrochemical performance of P2/O3 biphasic materials is enhanced in comparison to that of either the pure P2 phase or the pure O3 phase. Two potential scenarios can be postulated. The first is that the P2 and O3 phases in the hybrid material function in concert to provide capacity and amplify the advantages of the different phases. The second is that the O3 phase in the biphasic material remains inactive to stabilize the lattice. Despite the advancements made in the research of P2/O3 biphasic cathode materials, numerous challenges remain to be addressed. For instance, there is a lack of predictability in the synthesis conditions and a paucity of research into the underlying mechanisms. In the future research of layered biphasic cathode materials, the key lies in the exploration of controllable and precise synthesis methods and the provision of intuitive and in-depth mechanistic evidence. With regard to the synthesis conditions, single-phase materials are more likely to be formed under specific components, calcination temperatures, and atmospheres. In contrast, biphasic materials are usually formed under still uncertain intermediate conditions, which makes it difficult to fabricate biphasic materials with specific stoichiometric ratios. The study of the mechanism is not yet sufficiently comprehensive, and further characterisation tools, such as X-ray absorption fine structure, in situ transmission electron microscopy, and DFT, are required for a more in-depth investigation[103].

3.3 Surface coating

Constructing surface cladding layers is a well-established method for improving material stability and achieving excellent electrochemical properties.

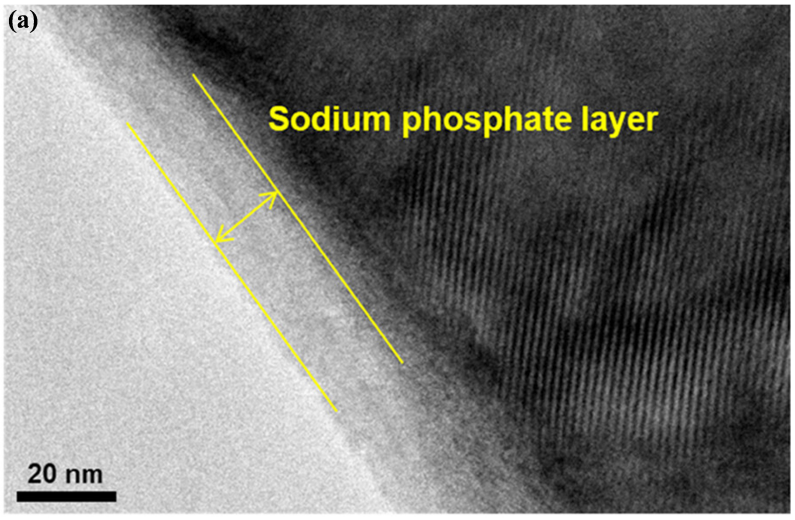

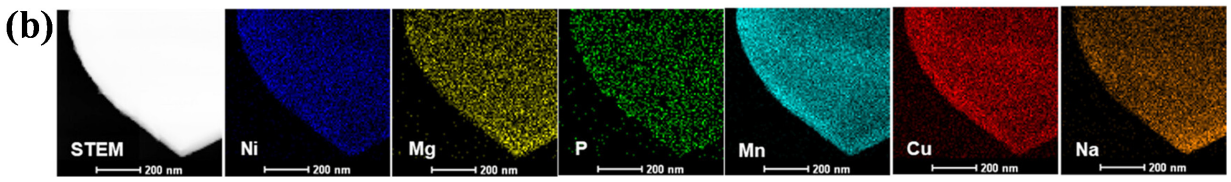

Fig 20. (a) TEM image of NMCM@P. (b) STEM image of NMCM@P and its element mapping. Reproduced with permission[104]. Copyright 2023, American Chemical Society.

Lee et al.[104] synthesized Na_3PO_4-coated $Na_{0.60}Ni_{0.17}Mg_{0.11}Cu_{0.06}Mn_{0.66}O_2$ (NMCM@P) cathode material. As shown in **Figure 20a**, the TEM image revealed a thin and uniform sodium phosphate layer with a 15 nm thickness on the surface of NMCM. The EDS elemental mapping demonstrated well-dispersed substituted cations in the particles, and uniform distribution of phosphorus on the particle surface (**Figure 20b**). The stability of the structure and cycling stability were improved by the sodium phosphate coating, which suppressed surface side reactions during charging and discharging. The capacity was increased by 48% at 4A g^{-1} compared to the uncoated sample, and the NMCM@P capacity retention was about 90% after 100 cycles.

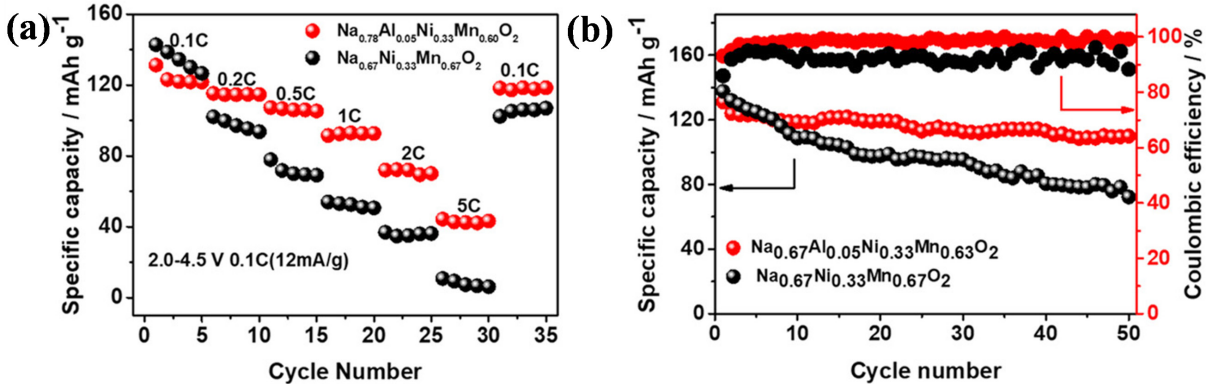

Fig 21. Electrochemical properties of $Na_{0.78}Al_{0.05}Ni_{0.33}Mn_{0.60}O_2$ and $Na_{0.66}Ni_{0.33}Mn_{0.67}O_2$ electrodes. (a) rate performance. (b) cycling performance. Reproduced with permission[105]. Copyright 2019, American Chemical Society.

Shi et al.[105] showed that by doping Al^{3+} on the basis of $Na_{0.66}Ni_{0.33}Mn_{0.67}O_2$, Al^{3+} did not completely enter the lattice, and part of the Al^{3+} was enriched on the surface of the material to form an Al_2O_3 capping layer. The P2-O2 phase transition and volume change, as well as the migration of cations, were suppressed, resulting in good rate performance and high capacity retention. As shown in **Figure 21a-b**, the discharge capacity of the $Na_{0.78}Al_{0.05}Ni_{0.33}Mn_{0.60}O_2$ electrode was 41.2 mAh g^{-1} in the voltage interval of 2-4.5 V at 5 C, while the capacity retention rate was 83.9% after 50 cycles at 0.1 C.

Xu et al.[106] reported the development of a surface-optimized high-rate P2-$Na_{2/3}Ni_{1/3}Mn_{2/3}O_2$(NM) cathode material coated with 1 wt % Al-doped ZnO (AZO) and a thickness of approximately 7.55 nm. The material was prepared by coating AZO at 500 °C. The construction of the AZO surface coating has a high electronic conductivity, which facilitates enhanced rate performance and reduced charge transfer resistance during the cycle. Concurrently, the direct electrode-electrolyte contact is prevented to safeguard the active cathode and mitigate the formation of surface cracks in the cathode throughout the cycle. The material exhibits good cycle and rate performance. As demonstrated in **Figure 22a-c**, the NM@AZO-500 cathode material exhibits a stable discharge capacity of 79.3 mAh g^{-1} at 5 C, which is markedly superior to that of the NM bare counterpart (56.9 mAh g^{-1}). After 500 cycles at 5 C, NM@AZO-500 continues to demonstrate a reversible discharge capacity of 66.2 mAh g^{-1} and a capacity retention of 82.6%, which is markedly superior to that of NM(47.4 mAh g^{-1} and 61.2%).

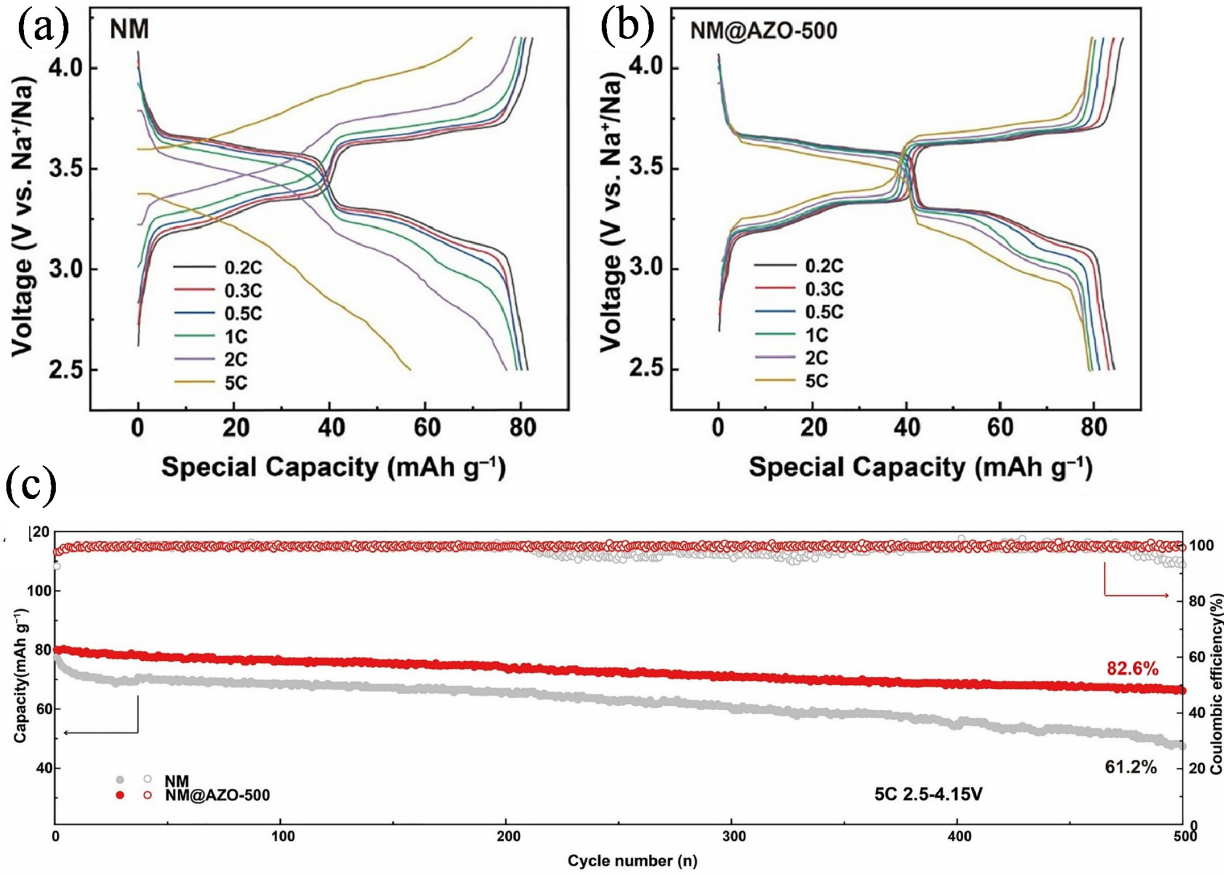

Fig 22. Rate performances of (a) NM and (b) NM@AZO-500 samples between 2.5 and 4.15 V. (c) Long-term cycling performances of the bare NM and NM@AZO-500 samples at 5 C between 2.5 and 4.15 V. Reproduced with permission[106]. Copyright 2022, Elsevier.

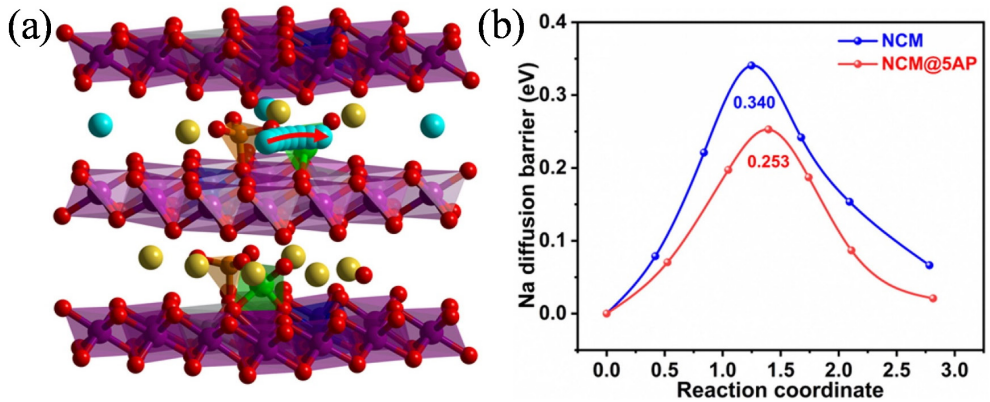

Fig 23. (a) Diffusion path of NCM@5AP cathode simulated by first-principles calculation (Mn: purple, Co: blue, Ni: grey, O: red, Na: yellow and cyan, Al: green, and P: orange). (b) The calculated migration energy barrier of Na^+ in pristine NCM and NCM@5AP electrodes. Reproduced with permission[107]. Copyright 2022, Elsevier.

Xiao et al.[107] prepared NCM@3AP, NCM@5AP, and NCM@7AP cathode materials by depositing protective layers with mass fractions of 3, 5, and 7 wt% amorphous aluminum phosphate (AlPO4, denoted as AP) on the surface of P2-type $Na_{0.55}Ni_{0.1}Co_{0.1}Mn_{0.8}O_2$ by wet chemical deposition. As illustrated in Fig. 23a-b, the energy barriers of NCM@5AP were found to be lower than those of the pristine NCM, thereby confirming that the surface modification could facilitate the diffusion rate of Na^+ ions. The coating

is an effective means of mitigating the Jahn-Teller effect of Mn^{3+} by reducing the amount of Mn^{3+} ions. The introduction of a 5 wt% AP coating (NCM@5AP) on the NCM cathode demonstrated a significant improvement in Na^+ kinetics and cycling stability compared to the pristine NCM. NCM@5AP exhibited a capacity retention of 78.4% after 200 cycles at 100 mA g^{-1} and an excellent rate performance of 98 mAh g^{-1} at 500 mA g^{-1}.

Previous research has demonstrated that surface coating is an effective method for enhancing the electrochemical performance of P2-type layered oxides. The primary objective of constructing a surface coating layer is to prevent the occurrence of side reactions in the direct contact between the cathode and electrolyte, thereby enhancing the interfacial stability. Furthermore, the application of a coating material or surface treatment method can result in enhanced electrochemical performance, including the promotion of Na^+ diffusion and the inhibition of damage phase transition. Notwithstanding the considerable progress that has been made in the development of surface coating strategies, a number of challenges remain. First, it is challenging to obtain uniform coating layers through non-in situ methods, which limits the effectiveness of the protective layer. Secondly, it is imperative to regulate the quantity of the coating material employed, particularly in the case of oxide coatings with inadequate electronic conductivity. Excessive coating can result in a rapid deterioration of the electrochemical performance, which is a significant obstacle to the commercialization of these materials[83]. The electrochemical performances of the layered oxide cathodes for SIBs are summarized in **Table 1**.

Table 1. Summary of the P2-Na_xTMO_2 electrodes materials for SIBs applications.

Materials	Voltage Range (vs. Na^+/Na)	Cyclic Stability	Rate Capability	Ref.
$Na_{2/3}Li_{0.1}Ni_{0.23}Mn_{0.67}O_2$	2.0-4.3 V	79.9% capacity retention at 0.1 C after 100 cycles	121.5 mAh g^{-1} at 0.1 C	[86]
$Na_{2/3}Li_{1/9}Ni_{2/9}Mn_{2/3}O_2$	2.5-4.15 V	78.7% capacity retention at 2 C after 300 cycles 71.7% capacity retention at 5 C after 300 cycles	97.6 mAh g^{-1} at 0.2 C 70.0 mAh g^{-1} at 5 C	[87]
$Na_{0.7}Li_{0.03}[Mg_{0.15}Li_{0.07}Mn_{0.75}]O_2$	1.5-4.6 V	80.9% capacity retention at 0.5 C after 50 cycles	266 mAh g^{-1} at 0.05 C 126 mAh g^{-1} at 5 C	[88]
$Na_{0.7}Mg_{0.05}[Mn_{0.6}Ni_{0.2}Mg_{0.2}]O_2$	1.5-4.2 V	79% capacity retention at 1 C after 100 cycles	74 mAh g^{-1} at 0.2 C 57 mAh g^{-1} at 25 C	[89]
$Na_{2/3}Ni_{1/3}Mn_{1/3}Ti_{1/3}O_2$	2.5-4.5 V	84.71% capacity retention at 1 C after 150 cycles	109.6 mAh g^{-1} at 1 C	[90]
$Na_{0.78}Ni_{0.31}Mn_{0.67}Nb_{0.02}O_2$	2.4-4.15 V	76% capacity retention at 368 mA g^{-1} after 1800 cycles	65 mAh g^{-1} at 50 C	[91]
$Na_{0.67}Ni_{0.18}Cu_{0.15}Mn_{0.67}O_2$	2-4.3 V	78% capacity retention at 0.1 C after 200 cycles	120 mAh g^{-1} at 0.1 C 62 mAh g^{-1} at 20 C	[92]
$Na_{2/3}Ni_{1/3}Mn_{2/3}O_{1.95}F_{0.05}$	2-4 V	89% capacity retention at 2 C after 400 cycles 75.6% capacity retention at 10 C after 2000 cycles	95.4 mAh g^{-1} at 2 C	[93]
$Na_{0.93}Li_{0.07}Cu_{0.07}Ni_{0.29}Mn_{0.57}O_2$	2-4.2 V	85% capacity retention at 0.2 C after 200 cycles	110 mAh g^{-1} at 0.2 C	[97]
$Na_{0.67}Ni_{0.29}Zn_{0.04}Mn_{0.63}Ti_{0.04}O_2$	2.5-4.3 V	67% capacity retention at 0.5 C after 300 cycles	125.6 mAh g^{-1} at 0.5 C	[98]
$Na_{0.67}Mn_{0.71}Cu_{0.02}Mg_{0.02}Ni_{0.25}O_2$	1.5-4.5 V	86% capacity retention at 0.1 C after 100 cycles	160 mAh g^{-1} at 0.05 C 152 mAh g^{-1} at 0.1 C 72 mAh g^{-1} at 10 C	[99]
$Na_{0.736}Ni_{0.264}Mg_{0.1}Mn_{0.636}O_2$	2.0-4.3 V	73.1% capacity retention at 1 C after 200 cycles	130 mAh g^{-1} at 0.1 C	[101]
$Na_{0.85}Ni_{0.34}Mn_{0.33}Ti_{0.33}O_2$	2.2–4.4 V	80.6% capacity retention at 1 C after 200 cycles	126.8 mAh g^{-1} at 0.1 C 82.4 mAh g^{-1} at 10 C	[102]
$Na_{0.60}Ni_{0.17}Mg_{0.11}Cu_{0.06}Mn_{0.66}O_2$ @Na_3PO_4	1.5-4.3 V	90% capacity retention at 0.1 A g^{-1} after 100 cycles	127 mAh g^{-1} at 0.05 A g^{-1} 121 mAh g^{-1} at 0.1 A g^{-1} 48 mAh g^{-1} at 4 A g^{-1}	[104]

Continuation Table:

Materials	Voltage Range (vs. Na^+/Na)	Cyclic Stability	Rate Capability	Ref.
$Na_{0.78}Al_{0.05}Ni_{0.33}Mn_{0.60}O_2$	2.0-4.5 V	83.9% capacity retention at 0.1 C after 50 cycles	123.9 mAh g^{-1} at 0.1 C 41.2 mAh g^{-1} at 5 C	[105]
NM@AZO-500	2.5-4.15 V	92.7% capacity retention at 1 C after 300 cycles 82.6% capacity retention at 5 C after 500 cycles	79.3 mAh g^{-1} at 5 C	[106]
NCM@5AP	1.5-4.3 V	78.4% capacity retention at 100 mA g^{-1} after 200 cycles	160 mAh g^{-1} at 20 mA g^{-1} 98 mAh g^{-1} at 500 mA g^{-1}	[107]

4. Prospects

A number of approaches have been developed with the objective of achieving an appropriate enhancement of the electrochemical properties of cathode materials for SIBs with a view to facilitating their commercialisation. Nevertheless, there is still a need to further explore advanced design routes and understand their mechanisms in order to improve their shortcomings and achieve commercial applications. In light of the findings presented in this review paper, it becomes evident that there is a need to integrate a number of key points in the material design and development of cathode materials for SIBs. Firstly, the structural stability of P2-type materials during charging and discharging has a significant impact on the cycling performance of SIBs. During the intercalation and de-intercalation of sodium, volume changes resulting from structural evolution and constant changes in stress occur, leading to the detachment of the active material from the electrode, which results in the degradation of properties such as specific capacity and cycling stability. Consequently, the synthesis of low-strain cathode materials and the suppression of volume change during the charging and discharging process have emerged as pivotal avenues in the design of cathode materials. In addition, the key issues require the suppression of structural distortion and the migration and dissolution of TMs due to the Jahn-Teller effect, which leads to geometrical distortion of the octahedra, which is detrimental to the structural stability and can affect the electrochemical properties of the materials. The Jahn-Teller effect is more likely to occur in octahedral complexes with Mn^{3+} in the high spin state, Ni^{3+} and Cu^{2+} in the low spin state. Therefore, it is important to avoid or reduce the amount of Jahn-Teller active elements or active valence ions at the design stage so that an extended cycle life can be achieved. In the high charging state, irreversible TM migration to the Na layer reduces the electrostatic repulsion between neighboring atoms in the TM layer, shrinks the spacing between the Na layers, and hinders the diffusion of Na^+. Consequently, the specific capacity of discharge and the cycle stability are decreased. The dissolution of elements with the Jahn-Teller effect (e.g., Mn^{3+} and Ni^{3+}) in the electrolyte results in the destruction of the electrolyte, anode, and cathode, and significantly impairs the electrochemical performance. The suppression of the structural distortion brought about by the Jahn-Teller effect and the migration and dissolution of transition metals to obtain stable structural materials and electrode interfaces enables the commercialization of cathode materials with long cycle life. In addition, during the charging and discharging processes, oxygen in the lattice may undergo redox reactions under certain conditions, resulting in the loss of electrons and the generation of additional capacity beyond the theoretical capacity. However, it should be noted that redox reactions are not always reversible in all materials, and irreversible oxygen redox, where lattice oxygen is irreversibly precipitated as O_2, may lead to transition metal migration and structural damage. It is evident that the realization of reversible oxygen redox can effectively address the deficiency in specific capacity exhibited by P2-type layered oxides, thereby satisfying the demand for anodes with high energy density in practical applications.

Elemental doping has been demonstrated to be an effective method for enhancing the electrochemical properties of cathode materials. Nevertheless, it is of paramount importance to ascertain whether this element can be employed as a suitable dopant for the active sites within the body component. Furthermore, multi-element doping represents an effective approach for the preparation of cathode materials. The atomic weight,

interactions, and electrochemical activities of different doping elements vary, and the collective influence of multiple elements on the electrochemical properties of cathode materials requires further investigation. In the context of energy storage systems, the most crucial performance index is high energy density. Given that the P2 phase is a sodium-deficient phase with a relatively small discharge specific capacity compared to the high sodium O3 phase, it is of particular importance to explore P2-type structural anode materials with high Na content by increasing the cation potential in order to facilitate the realization of commercial applications. Composites comprising P2 and O3 heterostructures exhibit enhanced electrochemical properties and greater stability. Nevertheless, despite some progress in P2/O3 heterostructured composites, there are still many aspects that are uncertain, such as the unpredictability of synthesis conditions and the proper distribution of proportions in various structures. A comprehensive investigation of the underlying mechanisms through the utilisation of advanced characterisation tools will facilitate the elucidation of the intrinsic relationship between the synthesis conditions and the specific ratios of the various structures, thereby paving the way for the discovery of novel P2/O3 materials with enhanced properties. Furthermore, the construction of a surface coating layer can prevent the occurrence of side reactions between the cathode and electrolyte and enhance interfacial stability, which represents an effective approach to enhance the electrochemical performance of P2-type layered oxides. Further exploration is required to identify methods for obtaining uniform coating layers and precisely controlling the coating amount of poorly electrically conductive oxide coatings by non-in situ methods. This is necessary for the practical preparation of surface coating materials. Comprehensive strategies are required to realize high-performance sodium-ion battery systems. Reviews of sodium-ion battery performance, including specific capacity, capacity retention, and number of cycles, are currently available. In addition to advances in cathode materials, the development of other features such as anodes, electrolytes, and separators is critical for the scale manufacturing of commercialized SIBs. Further understanding of the mechanisms, including structural changes, phase transitions, and charge compensation mechanisms, is necessary for the next studies. Based on the existing research progress, it can be reasonably assumed that the challenges and difficulties faced by large-scale commercial application of SIBs will be overcome soon.

5. Conclusions

In recent years, layered transition metal oxides have been widely studied as the most promising cathode materials for SIBs, and remarkable achievements and great progress have been made. Among them, P2-Na_xTMO_2 is considered to be one of the most likely commercialized layered transition metal oxide cathode materials due to its high theoretical capacity, high operating voltage, and good rate performance, and the P2-type layered materials usually have a high average operating voltage of 3.5-3.7 V. However, P2-Na_xTMO_2 cathode materials still face some challenges for practical applications. This review commences with a classification of cathode materials for SIBs. This is followed by a brief description of layered transition metal oxides, polyanionic compounds, and Prussian blue analogs. Thereafter, the structural classification of O3-type and P2-type cathode materials is discussed. Then, the problems of P2-Na_xTMO_2 cathode materials are summarized, such as irreversible phase transition at high voltage, Jahn-Teller aberration, irreversible oxygen atom redox, and transition metal migration and dissolution. Finally, the main current modification strategies are presented: (1) active or inactive single-element doping(Li, Mg, Cu, Al and Nb, etc.), (2) two-element doping(Li and Cu, Ti and Zn, etc.), (3) P2/O3 biphasic modification, and (4) surface coating. This work provides some theoretical guidance to further improve the electrochemical performance of P2-Na_xTMO_2 cathode materials. Although some significant advances have been made in the current research on P2-Na_xTMO_2 layered oxides, there are still some challenges that must be overcome for commercial viability. The primary objective of future research on P2-type layered oxides is to enhance specific energy. Primarily, the electrochemical performance, particularly the long-cycle performance, is inadequate for current practical applications and requires further enhancement. Secondly, although the P2 phase has a relatively open Na^+ migration path, its capacity is limited by the insufficient sodium content, and there is an urgent need to develop an efficient and low-

cost sodium replenishment technology to compensate for this shortcoming. The development of P2-type structures with elevated Na content through the enhancement of cation potential and the incorporation of elemental doping represents a promising avenue for future research on cathode materials with high energy density. Finally, the current study demonstrates that the formation of oxygen lone pair electrons or non-bonded oxygen states is not a prerequisite for anionic redox. Consequently, the reaction mechanism of this type of reaction requires further investigation in order to utilize the anionic redox reaction to further improve the specific capacity and cyclic stability. It is imperative to achieve reversible oxygen redox in order to obtain stable, commercially viable anode materials with high specific capacity. Furthermore, it is recommended that low-cost, eco-friendly, and non-toxic cathode candidates be considered for future research efforts in commercialized SIBs. Although numerous challenges remain to be overcome, P2-Na_xTMO_2, a class of cathode materials with higher energy densities, is believed to have the greatest potential to facilitate the commercialization of SIBs.

Declaration

Author's Contributions

Yu HR: Literature collection and research, writing & revising.

Li CP: Supervision, discussion, writing, review & revising.

Dong P: Funding acquisition, discussion.

Wang JS: Discussion.

Zhang ZF: Discussion, review & editing.

Zhang YJ: Funding acquisition, review & editing.

Chen JZ: Discussion, review & editing.

Conflict of Interest

The authors declare no competing financial interest.

Ethical approval and consent to participate

Not applicable.

Consent to publication

Not applicable.

Data Availability Statement

Supplementary materials at the end of the article.

Funding

The authors thank for the financial support of Yunnan Fundamental Research Projects (202201BE070001-019 and 202301AT070167) and Yunnan Major Scientific and Technological Projects (202202AG050003).

References

[1] Yadegari H, Sun XL. Recent advances on sodium-oxygen batteries: a chemical perspective. *Accounts of Chemical Research*, 2018; 51(6):1532-1540. https://doi.org/10.1021/acs.accounts.8b00139.

[2] Zhu XB, Wang LZ. Advances in materials for all-climate sodium-ion batteries. *EcoMat*, 2020; 2(3):e12043. https://doi.org/10.1002/eom2.12043.

[3] Lai X, Chen JJ, Chen QW, et al. Comprehensive assessment of carbon emissions and environmental impacts of sodium-ion batteries and lithium-ion batteries at the manufacturing stage. *Journal of Cleaner Production*, 2023; 423:138674. https://doi.org/10.1016/j.jclepro.2023.138674.

[4] Zhao Y, Liu Q, Zhao X, et al. Structure evolution of layered transition metal oxide cathode materials for Na-ion batteries: issues, mechanism and strategies. *Materials Today*, 2023; 62:271-295. https://doi.org/10.1016/j.mattod.2022.11.024.

[5] Dong F, Qin C, Zhang XY, et al. Towards carbon neutrality: the impact of renewable energy development on carbon emission efficiency. *International Journal of Environmental Research and Public Health*, 2021; 18(24):13284. https://doi.org/10.3390/ijerph182413284.

[6] Zhao LN, Zhang T, Li W, et al. Engineering of sodium-ion batteries: opportunities and challenges. *Engineering*, 2023; 24:172-183. https://doi.org/10.1016/j.eng.2021.08.032.

[7] Rabbi MF, Popp J, Máté D, et al. Energy security and energy transition to achieve carbon neutrality. *Energies*, 2022; 15(21):8126. https://doi.org/10.3390/en15218126.

[8] Palomares V, Serras P, Villaluenga I, et al. Na-ion batteries, recent advances and present challenges to become low cost energy storage systems. *Energy & Environmental Science*, 2012;

5(3):5884.
https://doi.org/10.1039/c2ee02781j.

[9] Liu TF, Zhang YP, Jiang ZG, et al. Exploring competitive features of stationary sodium ion batteries for electrochemical energy storage. *Energy & Environmental Science*, 2019; 12(5):1512-1533.
https://doi.org/10.1039/C8EE03727B.

[10] Hwang J-Y, Myung S-T, Sun Y-K. Sodium-ion batteries: present and future. *Chemical Society Reviews*, 2017; 46(12):3529-3614.
https://doi.org/10.1039/C6CS00776G.

[11] Pan HL, Hu Y-S, Chen LQ. Room-temperature stationary sodium-ion batteries for large-scale electric energy storage. *Energy & Environmental Science*, 2013; 6(8):2338.
https://doi.org/10.1039/c3ee40847g.

[12] Gao R-M, Zheng Z-J, Wang P-F, et al. Recent advances and prospects of layered transition metal oxide cathodes for sodium-ion batteries. *Energy Storage Materials*, 2020; 30:9-26.
https://doi.org/10.1016/j.ensm.2020.04.040.

[13] Xiao Y, Abbasi NM, Zhu Y, et al. Layered oxide cathodes promoted by structure modulation technology for sodium-ion batteries. *Advanced Functional Materials*, 2020; 30(30):2001334.
https://doi.org/10.1002/adfm.202001334.

[14] Yang H, Wang D, Liu YL, et al. Improvement of cycle life for layered oxide cathodes in sodium-ion batteries. *Energy & Environmental Science*, 2024; 17(5):1756-1780.
https://doi.org/10.1039/D3EE02934D.

[15] Larcher D, Tarascon J-M. Towards greener and more sustainable batteries for electrical energy storage. *Nature Chemistry*, 2015; 7(1):19-29.
https://doi.org/10.1038/nchem.2085.

[16] You Y, Manthiram A. Progress in high-voltage cathode materials for rechargeable sodium-ion batteries. A*dvanced Energy Materials*, 2018; 8(2):1701785.
https://doi.org/10.1002/aenm.201701785.

[17] Huang Z-X, Gu Z-Y, Heng Y-L, et al. Advanced layered oxide cathodes for sodium/potassium-ion batteries: development, challenges and prospects. *Chemical Engineering Journal*, 2023; 452:139438.
https://doi.org/10.1016/j.cej.2022.139438.

[18] Liu R, Liang ZT, Gong ZL, et al. Research progress in multielectron reactions in polyanionic materials for sodium-ion batteries. *Small Methods*, 2019; 3(4):1800221.
https://doi.org/10.1002/smtd.201800221.

[19] Hakim C, Sabi N, Saadoune I. Mixed structures as a new strategy to develop outstanding oxides-based cathode materials for sodium ion batteries: a review. *Journal of Energy Chemistry*, 2021; 61:47-60.
https://doi.org/10.1016/j.jechem.2021.02.027.

[20] Fang YJ, Zhang JX, Xiao L, et al. Phosphate framework electrode materials for sodium ion batteries. *Advanced Science*, 2017; 4(5):1600392.
https://doi.org/10.1002/advs.201600392.

[21] Oh G, Kim J, Kansara S, et al. Experimental and computational optimization of prussian blue analogues as high-performance cathodes for sodium-ion batteries: a review. *Journal of Energy Chemistry*, 2024; 93:627-662.
https://doi.org/10.1016/j.jechem.2024.02.013.

[22] Ling JK, Karuppiah C, Krishnan SG, et al. Phosphate polyanion materials as high-voltage lithium-ion battery cathode: a review. *Energy & Fuels*, 2021; 35(13):10428-10450.
https://doi.org/10.1021/acs.energyfuels.1c01102.

[23] Li HX, Xu M, Zhang ZA, et al. Engineering of polyanion type cathode materials for sodium-ion batteries: toward higher energy/power density. *Advanced Functional Materials*, 2020; 30(28):2000473.
https://doi.org/10.1002/adfm.202000473.

[24] Hao ZQ, Shi XY, Yang Z, et al. The distance between phosphate-based polyanionic compounds and their practical application for sodium-ion batteries. *Advanced Materials*, 2024; 36(7): 2305135.
https://doi.org/10.1002/adma.202305135.

[25] Qian JF, Wu C, Cao Y, et al. Prussian blue cathode materials for sodium-ion batteries and other ion batteries. *Advanced Energy Materials*, 2018; 8(17):1702619.
https://doi.org/10.1002/aenm.201702619.

[26] Wang W, Gang Y, Peng J, et al. Effect of eliminating water in prussian blue cathode for sodium-ion batteries. *Advanced Functional Materials*, 2022; 32(25):2111727.
https://doi.org/10.1002/adfm.202111727.

[27] Nie P, Yuan JR, Wang J, et al. Prussian blue analogue with fast kinetics through electronic coupling for sodium ion batteries. *ACS Applied Materials & Interfaces*, 2017; 9(24):20306-20312. https://doi.org/10.1021/acsami.7b05178.

[28] You Y, Wu X-L, Yin Y-X, et al. High-quality prussian blue crystals as superior cathode materials for room-temperature sodium-ion batteries. *Energy & Environmental Science*, 2014; 7(5):1643-1647. https://doi.org/10.1039/C3EE44004D.

[29] Liu QN, Hu Z, Chen MZ, et al. Recent progress of layered transition metal oxide cathodes for sodium-ion batteries. *Small*, 2019; 15(32):1805381. https://doi.org/10.1002/smll.201805381.

[30] Huang Z-X, Zhang X-L, Zhao X-X, et al. Hollow $Na_{0.62}K_{0.05}Mn_{0.7}Ni_{0.2}Co_{0.1}O_2$ polyhedra with exposed stable {001} facets and k riveting for sodium-ion batteries. *Science China Materials*, 2023; 66(1):79-87. https://doi.org/10.1007/s40843-022-2157-8.

[31] Huang Z-X, Zhang X-L, Zhao X-X, et al. Suppressing oxygen redox in layered oxide cathode of sodium-ion batteries with ribbon superstructure and solid-solution behavior. *Journal of Materials Science & Technology*, 2023; 160:9-17. https://doi.org/10.1016/j.jmst.2023.04.002.

[32] Zhang X-L, Huang Z-X, Liu Y-N, et al. Tuning oxygen release of sodium-ion layered oxide cathode through synergistic surface coating and doping. *Journal of Colloid and Interface Science*, 2023; 650:742-751. https://doi.org/10.1016/j.jcis.2023.06.201.

[33] Mathiyalagan K, Shin D, Lee Y-C. Difficulties, strategies, and recent research and development of layered sodium transition metal oxide cathode materials for high-energy sodium-ion batteries. *Journal of Energy Chemistry*, 2024; 90:40-57. https://doi.org/10.1016/j.jechem.2023.10.023.

[34] Delmas C, Fouassier C, Hagenmuller P. Structural classification and properties of the layered oxides. *Physica B+C*, 1980; 99(1-4):81-85. https://doi.org/10.1016/0378-4363(80)90214-4.

[35] Tournadre F, Croguennec L, Willmann P, et al. On the mechanism of the P2-$Na_{0.70}CoO_2$→O2-$LiCoO_2$ exchange reaction—part ii: an in situ X-ray diffraction study. *Journal of Solid State Chemistry*, 2004; 177(8):2803-2809. https://doi.org/10.1016/j.jssc.2004.04.028.

[36] Delmas C, Braconnier J-J, Hagenmuller P. A new variety of $LiCoO_2$ with an unusual oxygen packing obtained by exchange reaction. *Materials Research Bulletin*, 1982; 17(1):117-123. https://doi.org/10.1016/0025-5408(82)90192-1.

[37] Wang P, You Y, Yin Y, et al. Layered oxide cathodes for sodium-ion batteries: phase transition, air stability, and performance. *Advanced Energy Materials*, 2018; 8(8):1701912. https://doi.org/10.1002/aenm.201701912.

[38] Hwang J-Y, Myung S-T, Choi JU, et al. Resolving the degradation pathways of the O3-type layered oxide cathode surface through the nano-scale aluminum oxide coating for high-energy density sodium-ion batteries. *Journal of Materials Chemistry A*, 2017; 5(45):23671-23680. https://doi.org/10.1039/C7TA08443A.

[39] Liu H, Gao X, Chen J, et al. Cu-substitution P2-$Na_{0.66}Mn_{1-x}Cu_xO_2$ sodium-ion cathode with enhanced interlayer stability. *Journal of Energy Chemistry*, 2022; 75:478-485. https://doi.org/10.1016/j.jechem.2022.09.010.

[40] Zhao CL, Avdeev M, Chen LQ, et al. An O3-type oxide with low sodium content as the phase-transition-free anode for sodium-ion batteries. *Angewandte Chemie International Edition*, 2018; 57(24):7056-7060. https://doi.org/10.1002/anie.201801923.

[41] Zhao CL, Wang QD, Yao ZP, et al. Rational design of layered oxide materials for sodium-ion batteries. *Science*, 2020; 370(6517):708-711. https://doi.org/10.1126/science.aay9972.

[42] Pérez-Vicente C, Ariza R, Zuo W, et al. The magnesium insertion effects into P2-type $Na_{2/3}Ni_{1/3}Mn_{2/3}O_2$. *Small*, 2024; 20(8):2305690. https://doi.org/10.1002/smll.202305690.

[43] Cheng ZW, Zhao B, Guo Y, et al. Mitigating the large-volume phase transition of P2-type cathodes by synergetic effect of multiple ions for improved sodium-ion batteries. *Advanced Energy Materials*, 2022; 12(14):2103461. https://doi.org/10.1002/aenm.202103461.

[44] Kubota K, Kumakura S, Yoda Y, et al. Electrochemistry and solid-state chemistry of $NaMeO_2$ (Me = 3d transition metals). *Advanced*

Energy Materials, 2018; 8(17):1703415. https://doi.org/10.1002/aenm.201703415.

[45] Wang K, Yan PF, Sui ML. Phase transition induced cracking plaguing layered cathode for sodium-ion battery. *Nano Energy*, 2018; 54:148-155. https://doi.org/10.1016/j.nanoen.2018.09.073.

[46] Lu ZH, Dahn JR. In situ X-ray diffraction study of P2-$Na_{2/3}Ni_{1/3}Mn_{2/3}O_2$. *Journal of The Electrochemical Society*, 148(11): A1225-A1229.

[47] Li X, Ma XH, Su D, et al. Direct visualization of the jahn-teller effect coupled to Na ordering in $Na_{5/8}MnO_2$. *Nature Materials*, 2014; 13(6):586-592. https://doi.org/10.1038/nmat3964.

[48] Mortemard De Boisse B, Liu GD, Ma J, et al. Intermediate honeycomb ordering to trigger oxygen redox chemistry in layered battery electrode. *Nature Communications*, 2016; 7(1):11397. https://doi.org/10.1038/ncomms11397.

[49] Dang RB, Chen M, Li Q, et al. Na^+-conductive $Na_2Ti_3O_7$-modified P2-type $Na_{2/3}Ni_{1/3}Mn_{2/3}O_2$ via a smart in situ coating approach: suppressing Na^+/vacancy ordering and P2-O2 phase transition. ACS Applied Materials & Interfaces, 2019; 11(1):856-864. https://doi.org/10.1021/acsami.8b17976.

[50] Mao QJ, Yu Y, Wang J, et al. Mitigating the P2-O2 transition and Na^+/vacancy ordering in $Na_{2/3}Ni_{1/3}Mn_{2/3}O_2$ by anion/cation dual-doping for fast and stable Na^+ insertion/extraction. Journal of Materials Chemistry A, 2021; 9(17):10803-10811. https://doi.org/10.1039/D1TA01433A.

[51] Yao H-R, Lv W-J, Yuan X-G, et al. New insights to build Na^+/vacancy disordering for high-performance P2-type layered oxide cathodes. *Nano Energy*, 2022; 97:107207. https://doi.org/10.1016/j.nanoen.2022.107207.

[52] Wang P-F, Yao H-R, Liu X-Y, et al. Na^+/vacancy disordering promises high-rate Na-ion batteries. *SCIENCE ADVANCES*, 2018; 4(3):eaar6018.

[53] Wang YS, Xiao RJ, Hu Y-S, et al. P2-$Na_{0.6}[Cr_{0.6}Ti_{0.4}]O_2$ cation-disordered electrode for high-rate symmetric rechargeable sodium-ion batteries. *Nature Communications*, 2015; 6(1):6954. https://doi.org/10.1038/ncomms7954.

[54] Halcrow MA. Jahn-teller distortions in transition metal compounds, and their importance in functional molecular and inorganic materials. *Chemical Society Reviews*, 2013; 42(4):1784-1795. https://doi.org/10.1039/C2CS35253B.

[55] Freitag R, Conradie J. Understanding the Jahn-Teller effect in octahedral transition-metal complexes: a molecular orbital view of the Mn (β-diketonato)$_3$ complex. *Journal of Chemical Education*, 2013; 90(12):1692-1696. https://doi.org/10.1021/ed400370p.

[56] Jung H, Kim J, Kim S. Phonon study of Jahn-Teller distortion and phase stability in $NaMnO_2$ for sodium-ion batteries. Journal of Applied Physics, 2022; 132(5):055101. https://doi.org/10.1063/5.0086903.

[57] Conradie J. Jahn-Teller effect in high spin d4 and d9 octahedral metal-complexes. *Inorganica Chimica Acta*, 2019; 486:193-199. https://doi.org/10.1016/j.ica.2018.10.040.

[58] Zhang L, Wang CC, Liu YC, et al. Suppressing interlayer-gliding and Jahn-teller effect in P2-type layered manganese oxide cathode via Mo doping for sodium-ion batteries. *Chemical Engineering Journal*, 2021; 426:130813. https://doi.org/10.1016/j.cej.2021.130813.

[59] Fang H, Ji HC, Zhai JJ, et al. Mitigating Jahn-Teller effect in layered cathode material via interstitial doping for high-performance sodium-ion batteries. *Small*, 2023; 19(35):2301360. https://doi.org/10.1002/smll.202301360.

[60] Maitra U, House RA, Somerville JW, et al. Oxygen redox chemistry without excess alkali-metal ions in $Na_{2/3}[Mg_{0.28}Mn_{0.72}]O_2$. Nature Chemistry, 2018; 10(3):288-295. https://doi.org/10.1038/nchem.2923.

[61] Assat G, Tarascon J-M. Fundamental understanding and practical challenges of anionic redox activity in Li-ion batteries. *Nature Energy*, 2018; 3(5):373-386. https://doi.org/10.1038/s41560-018-0097-0.

[62] Tarascon JM, Vaughan G, Chabre Y, et al. In situ structural and electrochemical study of $Ni_{1-x}Co_xO_2$ metastable oxides prepared by soft chemistry. *Journal of Solid State Chemistry*, 1999; 147(1):410-420.

https://doi.org/10.1006/jssc.1999.8465.
[63] Kalyani P, Chitra S, Mohan T, et al. Lithium metal rechargeable cells using Li_2MnO_3 as the positive electrode. *Journal of Power Sources*, 1999; 80(1-2):103-106. https://doi.org/10.1016/S0378-7753(99)00066-X.
[64] Robertson AD, Bruce PG. Mechanism of electrochemical activity in Li_2MnO_3. *Chemistry of Materials*, 2003; 15(10):1984-1992. https://doi.org/10.1021/cm030047u.
[65] Saubanère M, McCalla E, Tarascon J-M, et al. The intriguing question of anionic redox in high-energy density cathodes for Li-ion batteries. *Energy & Environmental Science*, 2016; 9(3):984-991. https://doi.org/10.1039/C5EE03048J.
[66] Li M, Liu TC, Bi X, et al. Cationic and anionic redox in Lithium-ion based batteries. *Chemical Society Reviews*, 2020; 49(6):1688-1705. https://doi.org/10.1039/C8CS00426A.
[67] Liu JT, Kan WH, Ling CD. Insights into the high voltage layered oxide cathode materials in sodium-ion batteries: structural evolution and anion redox. *Journal of Power Sources*, 2021; 481:229139. https://doi.org/10.1016/j.jpowsour.2020.229139.
[68] Cui T, Li X, Fu Y. Anionic redox in rechargeable batteries: mechanism, materials, and characterization. *Advanced Functional Materials*, 2023; 33(41):2303191. https://doi.org/10.1002/adfm.202303191.
[69] Manthiram A. A reflection on Lithium-ion battery cathode chemistry. *Nature Communications*, 2020; 11(1):1550. https://doi.org/10.1038/s41467-020-15355-0.
[70] Seo D-H, Lee J, Urban A, et al. The structural and chemical origin of the oxygen redox activity in layered and cation-disordered Li-excess cathode materials. *Nature Chemistry*, 2016; 8(7):692-697. https://doi.org/10.1038/nchem.2524.
[71] Rong XH, Hu EY, Lu YX, et al. Anionic redox reaction-induced high-capacity and low-strain cathode with suppressed phase transition. *Joule*, 2019; 3(2):503-517. https://doi.org/10.1016/j.joule.2018.10.022.
[72] Rong XH, Liu J, Hu EY, et al. Structure-induced reversible anionic redox activity in Na layered oxide cathode. *Joule*, 2018; 2(1):125-140. https://doi.org/10.1016/j.joule.2017.10.008.
[73] Yabuuchi N, Hara R, Kubota K, et al. A new electrode material for rechargeable sodium batteries: P2-type $Na_{2/3}[Mg_{0.28}Mn_{0.72}]O_2$ with anomalously high reversible capacity. *Journal of Materials Chemistry A*, 2014; 2(40):16851-16855. https://doi.org/10.1039/C4TA04351K.
[74] Mortemard De Boisse B, Reynaud M, Ma J, et al. Coulombic self-ordering upon charging a large-capacity layered cathode material for rechargeable batteries. *Nature Communications*, 2019; 10(1): 2185. https://doi.org/10.1038/s41467-019-09409-1.
[75] Perez AJ, Batuk D, Saubanère M, et al. Strong oxygen participation in the redox governing the structural and electrochemical properties of Na-rich layered oxide Na_2IrO_3. Chemistry of Materials, 2016; 28(22): 8278-8288. https://doi.org/10.1021/acs.chemmater.6b03338.
[76] Nanba Y, Iwao T, Boisse BMD, et al. Redox potential paradox in Na_XMO_2 for sodium-ion battery cathodes. *Chemistry of Materials*, 2016; 28(4):1058-1065. https://doi.org/10.1021/acs.chemmater.5b04289.
[77] Zhang Y, Wu M, Ma JW, et al. Revisiting the $Na_{2/3}Ni_{1/3}Mn_{2/3}O_2$ cathode: oxygen redox chemistry and oxygen release suppression. *ACS Central Science*, 2020; 6(2):232-240. https://doi.org/10.1021/acscentsci.9b01166.
[78] Zuo WH, Ren FC, Li Q, et al. Insights of the anionic redox in P2-$Na_{0.67}Ni_{0.33}Mn_{0.67}O_2$. *Nano Energy*, 2020; 78:105285. https://doi.org/10.1016/j.nanoen.2020.105285.
[79] Rahman MM, Lin F. Oxygen redox chemistry in rechargeable Li-ion and Na-ion batteries. *Matter*, 2021; 4(2):490-527. https://doi.org/10.1016/j.matt.2020.12.004.
[80] Rynearson L, Antolini C, Jayawardana C, et al. Speciation of transition metal dissolution in electrolyte from common cathode materials. *Angewandte Chemie*, 2024; 136(5):e202317109. https://doi.org/10.1002/ange.202317109.
[81] Chu SY, Kim D, Choi G, et al. Revealing the origin of transition-metal migration in layered sodium-ion battery cathodes: random Na extraction and Na-free layer formation. *Angewandte Chemie*, 2023; 135(12):e202216174. https://doi.org/10.1002/ange.202216174.

[82] Silván B, Gonzalo E, Djuandhi L, et al. On the dynamics of transition metal migration and its impact on the performance of layered oxides for sodium-ion batteries: $NaFeO_2$ as a case study. *Journal of Materials Chemistry A*, 2018; 6(31):15132-15146. https://doi.org/10.1039/C8TA02473A.

[83] Liu W, Li JX, Li W, et al. Inhibition of transition metals dissolution in cobalt-free cathode with ultrathin robust interphase in concentrated electrolyte. *Nature Communications*, 2020; 11(1):3629. https://doi.org/10.1038/s41467-020-17396-x.

[84] Xing LD, Borodin O. Oxidation induced decomposition of ethylene carbonate from DFT calculations - importance of explicitly treating surrounding solvent. *Physical Chemistry Chemical Physics*, 2012; 14(37):12838. https://doi.org/10.1039/c2cp41103b.

[85] Asl HY, Manthiram A. Reining in dissolved transition-metal ions. *Science*, 2020; 369(6500): 140-141. https://doi.org/10.1126/science.abc5454.

[86] Chen Y, Su GB, Cheng X, et al. Electrochemical performances of P2-$Na_{2/3}Ni_{1/3}Mn_{2/3}O_2$ doped with Li and Mg for high cycle stability. Journal of Alloys and Compounds, 2021; 858:157717. https://doi.org/10.1016/j.jallcom.2020.157717.

[87] Li S, Xiao Y, Zhu Y-F, et al. A Li-substituted hydrostable layered oxide cathode material with oriented stacking nanoplate structure for high-performance sodium-ion battery. *Chemical Engineering Journal*, 2021; 412:128719. https://doi.org/10.1016/j.cej.2021.128719.

[88] Wu ZH, Ni YX, Tan S, et al. Realizing high capacity and zero strain in layered oxide cathodes via Lithium dual-site substitution for sodium-ion batteries. *Journal of the American Chemical Society*, 2023; 145(17):9596-9606. https://doi.org/10.1021/jacs.3c00117.

[89] Wang Q-C, Meng J-K, Yue X-Y, et al. Tuning P2-structured cathode material by Na-site Mg substitution for Na-ion batteries. *Journal of the American Chemical Society*, 2019; 141(2):840-848. https://doi.org/10.1021/jacs.8b08638.

[90] Zhong X-B, He C, Gao F, et al. In situ raman spectroscopy reveals the mechanism of titanium substitution in P2-$Na_{2/3}Ni_{1/3}Mn_{2/3}O_2$: cathode materials for sodium batteries. *Journal of Energy Chemistry*, 2021; 53:323-328. https://doi.org/10.1016/j.jechem.2020.05.018.

[91] Shi QH, Qi RJ, Feng XC, et al. Niobium-doped layered cathode material for high-power and low-temperature sodium-ion batteries. *Nature Communications*, 2022; 13(1):3205. https://doi.org/10.1038/s41467-022-30942-z.

[92] Yang L, Luo S-H, Wang YF, et al. Cu-doped layered P2-type $Na_{0.67}Ni_{0.33-x}Cu_xMn_{0.67}O_2$ cathode electrode material with enhanced electrochemical performance for sodium-ion batteries. *Chemical Engineering Journal*, 2021; 404:126578. https://doi.org/10.1016/j.cej.2020.126578.

[93] Liu K, Tan S, Moon J, et al. Insights into the enhanced cycle and rate performances of the F-substituted P2-type oxide cathodes for sodium-ion batteries. *Advanced Energy Materials*, 2020; 10(19):2000135. https://doi.org/10.1002/aenm.202000135.

[94] Lun ZY, Ouyang B, Kitchaev DA, et al. Improved cycling performance of Li-excess cation-disordered cathode materials upon fluorine substitution. *Advanced Energy Materials*, 2019; 9(2):1802959. https://doi.org/10.1002/aenm.201802959.

[95] Chen H, Wu ZG, Zhong YJ, et al. Boosting the reactivity of Ni^{2+}/Ni^{3+} redox couple via fluorine doping of high performance $Na_{0.6}Mn_{0.95}Ni_{0.05}O_{2-x}F_x$ cathode. *Electrochimica Acta*, 2019; 308:64-73. https://doi.org/10.1016/j.electacta.2019.04.003.

[96] Piao J-Y, Gu L, Wei ZX, et al. Phase control on surface for the stabilization of high energy cathode materials of Lithium ion batteries. *Journal of the American Chemical Society*, 2019; 141(12):4900-4907. https://doi.org/10.1021/jacs.8b13438.

[97] Anilkumar A, Nair N, Nair SV, et al. Tailoring high Na content in P2-type layered oxide cathodes via CuLi dual doping for sodium-ion batteries. *Journal of Energy Storage*, 2023; 72:108291. https://doi.org/10.1016/j.est.2023.108291.

[98] Chen D, Zhang HL, Yang HY, et al. Promoting Na-ion storage in P2-$Na_{0.67}Ni_{0.33}Mn_{0.67}O_2$ cathode via synergetic Ti and Zn co-incorporation. *Applied*

Physics Letters, 2024; 124(8):083904. https://doi.org/10.1063/5.0188032.

[99] Kong WJ, Gao R, Li QY, et al. Simultaneously tuning cationic and anionic redox in a P2-$Na_{0.67}Mn_{0.75}Ni_{0.25}O_2$ cathode material through synergic Cu/Mg co-doping. *Journal of Materials Chemistry A*, 2019; 7(15): 9099-9109. https://doi.org/10.1039/C9TA00968J.

[100] Peng B, Wan GL, Ahmad N, et al. Recent progress in the emerging modification strategies for layered oxide cathodes toward practicable sodium ion batteries. *Advanced Energy Materials*, 2023; 13(27):2300334. https://doi.org/10.1002/aenm.202300334.

[101] Zhang L, Guan C, Zheng J, et al. Rational design of intergrowthP2/O3 biphasic layered structure with reversible anionic redox chemistry and structural evolution for Na-ions batteries. *Science Bulletin*, 2023; 68(2):180-191. https://doi.org/10.1016/j.scib.2023.01.010.

[102] Yu LZ, Cheng ZW, Xu K, et al. Interlocking biphasic chemistry for high-voltage P2/O3 sodium layered oxide cathode. *Energy Storage Materials*, 2022; 50:730-739. https://doi.org/10.1016/j.ensm.2022.06.012.

[103] Wang Q, Chu SY, Guo SH. Progress on multiphase layered transition metal oxide cathodes of sodium ion batteries. *Chinese Chemical Letters*, 2020; 31(9):2167-2176. https://doi.org/10.1016/j.cclet.2019.12.008.

[104] Lee SY, Kim YS, Park S, et al. Effect of sodium phosphate coating on Cu and Mg-substituted P2-$Na_{0.67}Ni_{0.33}Mn_{0.67}O_2$ for improving the cycling performance of sodium-ion capacitors. *ACS Applied Materials & Interfaces*, 2023; 15(47):54530-54538. https://doi.org/10.1021/acsami.3c13351.

[105] Shi YS, Li S, Gao A, et al. Probing the structural transition kinetics and charge compensation of the P2-$Na_{0.78}Al_{0.05}Ni_{0.33}Mn_{0.60}O_2$ cathode for sodium ion batteries. *ACS Applied Materials & Interfaces*, 2019; 11(27):24122-24131. https://doi.org/10.1021/acsami.9b06233.

[106] Xu K, Yan MM, Chang Y-X, et al. Surface optimized P2-$Na_{2/3}Ni_{1/3}Mn_{2/3}O_2$ cathode material via conductive al-doped zno for boosting sodium storage. *Electrochimica Acta*, 2022; 419:140394. https://doi.org/10.1016/j.electacta.2022.140394.

[107] Xiao J, Xiao Y, Wang S, et al. Surface engineering of P2-type cathode material targeting long-cycling and high-rate sodium-ion batteries. *Journal of Energy Chemistry*, 2024; 97:444-452. https://doi.org/10.1016/j.jechem.2024.06.007.